Vilnius University

Faculty of Physics
Laser Research Center

Abhinay Vats Mohan

Fabrication of Opaque 3D Microstructures using Multiphoton Lithography and their Characterization

Master Thesis

Lasers And Optical Technologies

Supervisor	Prof. Mangirdas Malinauskas
Consultant	Dr. Greta Merkininkaitė
Reviewer	Dr. Darius Gailevičius
LRC Director	Dr. Dalia Kaškelytė

Vilnius 2026

Contents

Introduction

Laser Direct Writing (LDW) is an additive manufacturing technique (AM), [1] in which a focused laser beam selectively modifies or deposits material with high spatial precision [2]. In contrast to conventional lithographic techniques that often rely on masks and molds, LDW enables direct pattern generation from computer-designed models, allowing rapid prototyping and fabrication of complex free-form geometries. By selectively deflecting the laser beam or the substrate, material can be added or transformed with point-by-point precision, to create two-dimensional and three-dimensional structures. Owing to its capacity for rapid prototyping, high resolution and large design flexibility, LDW has found applications in microelectronics [3], microoptics [4], metasurfaces [5], microfluidics [6], photonic devices [7] and various other fields of science and technology.

Out of a myriad of different laser writing techniques [8], Two-Photon Polymerization (TPP) [9], (also referred to as Two-Photon Lithography (TPL), Multiphoton Lithography (MPL), Multiphoton Absorption (MPA), Multiphoton 3D Lithography (MP3DL) etc), has gained significant attention due to its ability to achieve high resolution fabrication and its compatibility with a wide range of photopolymer resins. The application of TPP has increased considerably, especially following the advent and rapid development of femtosecond lasers. The high intensities achieved with such lasers allow nonlinear light-matter interactions to occur at the tightly focused spot, leading to multiphoton absorption in the photoresist [10]. This process initiates a photochemical reaction, creating changes in the bond structure of the resist within the exposed volume and enabling the fabrication of complex, arbitrarily shaped 3D micro- and nanostructures. Due to the high degree of control, precision and resolution offered by this technique, it has been widely employed for the fabrication of photonic devices [7], microoptics [4] and microelectronics [3].

Despite its versatility, the microstructures fabricated using TPP are predominantly polymeric and transparent in nature [11]. This transparency arises from the absence of significant absorbing or scattering centers in the polymerized resin, within the visible and infrared spectral ranges. Since TPP enables free-form fabrication, various optically transparent devices such as microlenses [12], diffractive optical elements (DOEs) [13], micro-mirrors [14], waveguides [15] and other integrated photonic devices [16] have been realized using this technique. While transparency is advantageous, optical systems also require opaque and mechanically robust components, such as apertures and beam blockers, for stray light suppression, optical filtering, and beam absorption. However, such opaque microstructures remain relatively unexplored in the context of TPP [17]. The primary reason is that photopolymerization of opaque resins is significantly more challenging due to strong light absorption in the UV to the near-infrared regime. In this work, a novel hybrid resin that produces optically opaque microstructures post pyrolysis is demonstrated.

To develop opaque microstructures suitable for micro-optical applications, additional material requirements must be satisfied, including high material hardness, high damage thresholds, chemical inertness and non-reactive behavior. These requirements motivate the fabrication of inorganic 3D microstructures [18] which offer exceptional mechanical and optoelectronic properties, while remaining structurally compact. However, their fabrication presents several challenges such as reduced resolution due to scattering and absorption of light by the larger ceramic particles, restricting the resolution to several micrometers and even larger [19], causing a significant increase in the feature sizes, limited compatibility with photoresists due to restricted material diversity and poor structural dimensions, often showcasing poor structural fidelity, cracking and deformations [20]. To address this, hybrid organic-inorganic resists are used as precursors for 3D ceramic microstructures [21]. Recent advances in material synthesis have enabled the development of homogeneous hybrid organic-inorganic resins suitable for multiphoton 3D lithography (MP3DL), overcoming many limitations of traditional ceramic fabrication methods [22]. These resins combine photopolymerizable organic backbones with inorganic networks.

The main goal of this study is to fabricate true 3D microstructures using a hybrid organic-inorganic resist via multiphoton lithography and to characterize their optical opacity after pyrolysis.

The tasks set to achieve this goal are the following:

1. To systematically determine the optimal laser fabrication window by varying laser power and scanning velocity by fabricating arrays of structures, in order to identify the correct parameter ranges that lead to the fabrication of structures that survive the development process without any deformations.

2. To fabricate and develop stable and bulky 3D microstructures using the optimized laser parameters and to verify their structural integrity using the optical microscope and optical profilometer.

3. To carry out the pyrolysis process at high temperatures to eliminate the organic components and obtain truly inorganic and opaque microstructures.

4. To characterize the anisotropic shrinkage and surface quality post pyrolysis by measuring dimensional changes along the axes and analyzing surface quality using optical profilometer.

5. To observe the decreased optical transmission of the resulting opaque inorganic microstructures post pyrolysis and assess their future application in microoptics.

1 Literature Review

1.1 Photopolymerization

Photopolymerization is a light-induced chemical process in which incident photons are absorbed by a photoresist, leading to changes in its solubility and mechanical properties [23] [24]. Depending on the type of response, photoresists are classified into two categories: positive and negative resists. Positive-tone resists undergo bond cleavage upon photon absorption, resulting in an increase in the solubility of the exposed regions. In contrast, negative-tone resists undergo cross-linking of monomers and oligomers present in the resist to form long polymer chains, which decrease the solubility of the exposed material.

The photopolymerization process can also be classified based on the reactive species responsible for polymer chain propagation within the resist. Accordingly, it is broadly divided into radical and cationic photopolymerization. Radical polymerization is initiated by free radicals generated through the absorption of incident photons. These radicals react with carbon-carbon double bonds (C=C), typically present in acrylate and methacrylate groups, leading to chain growth via the successive addition of monomers. In contrast, cationic photopolymerization is initiated by photoacid generation, which activates monomers such as epoxies through ionic mechanisms.

$$\text{Photoacid Generator (PAG)} \xrightarrow{h\nu} \text{Strong Acid } (H^+)$$

The acid opens ring structures that allow the polymeric chains to grow via ionic mechanisms, thus here the process is driven by cations in contrast to radicals.

The radical photopolymerization process can be described in the following steps:

1. **Initiation:** It is the first step of the photopolymerization process, where the nonlinear absorption of two or more photons by the photosensitive resin leads to generation of radicals.

$$PI \xrightarrow{h\nu} PI^* \longrightarrow R^* \tag{1}$$

$$R^* + M_1 \longrightarrow RM_1^* \tag{2}$$

2. **Propagation**: After the radical generation, they interact with the monomers in the resist to form new molecules that consist of free bonds. The chain continues to propagate, where the radicals react with monomers to generate new reactive species, and unreacted monomers continue to attach to the chain, leading to the cross-linking of such monomeric elements to form long polymeric chains. As the polymer chain con-

tinues to elongate rapidly, the excitation energy is no longer required for this process.

$$RM_1^* + M_2 \longrightarrow RM_1M_2^* \tag{3}$$

$$RM_1 \cdot .. M_n^* + M_k \longrightarrow RM_{n+k}^* \tag{4}$$

3. **Termination:** The elongation process of the polymer chain continues until a free radical attaches to an available free bond, or if another polymer chain with a free linkage is attached. This process is also terminated when the elongating polymer chain reacts with oxygen atoms, a process which is termed as quenching. Oxygen atoms readily react with the active radical species to form peroxy radicals, which are too stable to initiate new chain growth, effectively killing the propagation chain.

$$RM_{n+k}^* + R^* \longrightarrow RM_{n+k}R \tag{5}$$

$$RM_n^* + RM^* \longrightarrow RM_nM_mR \tag{6}$$

Here ***PI*** denotes 'photoinitiator', a specific chemical compound added to a resin consisting of monomers and oligomers. This photoinitiator has low photodissociation energy, which increases the photosensitivity of the resin. ***R*** refers to 'radical', which is generated after the absorption of incident photons by the photosensitive resist, and ***M*** refers to 'monomers', which are smaller organic molecules (consisting of carbon and hydrogen bonds) that can bond together to form larger chains of macromolecules. During the photopolymerization process, when a high-intensity laser beam is focused into a photosensitive resin, nonlinear light-matter interactions occur, leading to multiphoton absorption (MPA), in which two or more photons are absorbed simultaneously by a molecule. The optical nonlinearity induced by short, intense pulses alters the relationship between the absorption rate and the incident intensity. In this regime, the absorption rate becomes proportional to the square (or higher powers) of the light intensity, resulting in highly localized energy deposition [25]. Upon photon absorption, molecules are excited from the ground state S_0 to higher-energy singlet states (e.g.,S_1). Once excited, the molecule can relax through multiple pathways, each corresponding to a distinct physical process, as illustrated in Fig. 1 [26].

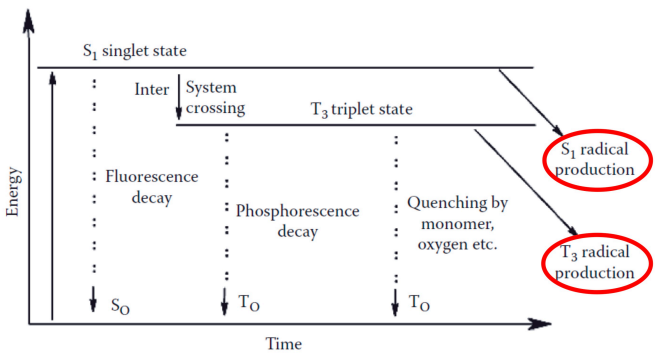

Figure 1: Jablonski Diagram of Energy vs Time. Reproduced from [27]

1.2 Hybrid Resin and Sol-Gel Chemistry

Ceramic structures are of great importance in various fields of science and technology due to their exceptional material properties. They are employed in components that can survive extreme conditions such as high stresses, high temperatures and chemically active environments. Such ceramic materials have been manufactured over the years using different techniques, such as slurry based techniques (employed in stereolithography [28] [29], direct ink writing [30], injection printing [31] and digital light processing [32]) and powder based techniques [33] (employed in selective laser sintering and melting [34]). Although these manufacturing techniques lead to successful fabrication of true ceramic materials, the main drawback of such techniques is the low resolution that is achieved for the structures, thus rendering such methods unsuitable for fabrication of photonic and optical elements at the microscale. The main reason for the low resolution is found to be in the manufacturing technique itself, which involves the dispersion of inorganic ceramic particles in an organic resist. Such particle-loaded resins suffer agglomeration, leading to non-uniform distribution of the inorganic phase, which adversely affects the final polymer. This creates an unstable and non-transparent resin, causing the laser light to be scattered or absorbed during the polymerization process, leading to unintentional changes in the morphology of the printed structures. In order to overcome such issues, hybrid resins were developed.

Hybrid resins, especially homogeneous hybrid organic-inorganic resins combines photopolymerizable organic components with inorganic network forming precursors, providing a versatile approach to the construction of inorganic microstructures [35]. The most commonly used inorganic framework for such structures is silicon oxide, but they can also include carbonates, phosphates, and chalcogenides [36]. Such resins are often synthesized via sol-gel process, utilizing organosilanes or metal alkoxides, in combination with organic monomers, such as acrylates and epoxies as precursors for the structures. The hybrid resin employed in this study consists of two monomers, MTMS (Methyltrimethoxysilane) and MAPTMS (3-(Trimethoxysilyl)propyl methacrylate) in a ratio of 8:2 (MTMS:MAPTMS) [37]. MAPTMS contains the methacrylate functional group that enables free radical photopolymerization under laser exposure, which leads to cross-linking of the organic monomers to form polymeric chains. This acrylate group is thus responsible for the negative tone behavior of the resist. MTMS on the other hand acts as the inorganic network former, and it does not participate in the radical polymerization process, but instead provides the necessary inorganic silicon-oxygen backbone, and yields the ceramic structure after the thermal treatment, thus acting as the ceramic precursor component of the photoresist. The photoinitiator added to this resin to increase the photosensitivity of the resin and the efficiency of photon absorption is Irgacure 369 (IRG) (2-benzyl-2-dimethylamino-1-(4- morpholinophenyl)-butanone-1), which is a radical photoinitiator.

The preparation of a hybrid resin generally involves the employment of the sol-gel process, which is a method used for the preparation of metallic oxides, especially silicon oxides. The process involves the conversion of the monomers in the solution into a colloidal solution (sol), that acts as a precursor to an integrated network of polymers (gel) or even discrete particles [38]. The synthesis of a hybrid resin using the sol-gel process starts with hydrolysis, whereby the alkoxysilanes in the monomers react with water, to form an OH group (silanol). Prior to the hydrolysis process the alkoxysilane molecules exist as discrete molecular species, which are isolated and stable in nature, with no individual ability to form solid networks. However the hydrolysis process produces the silanols which form reactive bonding species, ready to form solid networks. The next step of the sol-gel process involves condensation, where the real transition from sol to gel occurs. The condensation process aids in the transition of the resin into a gel, where condensation eliminates the hydroxyl groups forming siloxane (Si-O-Si) bonds. The formation of this solid network provides the gel-like viscosity to the resin, making it suitable for the photopolymerization process.

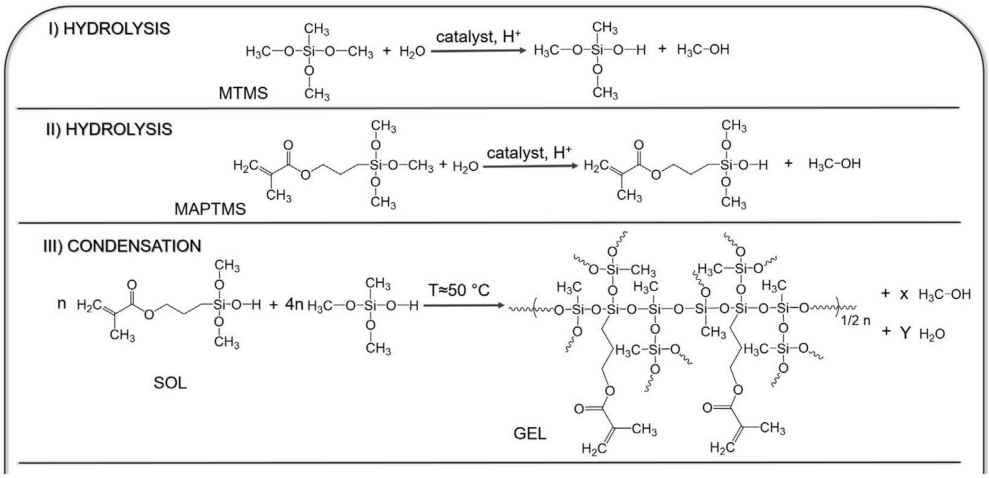

Figure 2: Schematic diagram showing the sol-gel process used for material synthesis via the following steps: I) Hydrolysis of MTMS and II) MAPTMS, followed by III) Mixing and condensation. Adapted from [37]

In this specific resin, MTMS and MAPTMS were individually hydrolysed with aqueous hydrochloric acid solution at 1:1 molar ratio. The solution of the alkoxysilane and water becomes homogeneous after 30 minutes of continuous stirring, indicating the successful hydrolysis of the groups. During the next step, hydrolyzed MAPTMS was added drop-wise to hydrolyzed MTMS solution, followed by the addition of the photoinitiator Irgacure 369 (IRG) (2-benzyl-2-dimethylamino-1-(4- morpholinophenyl)-butanone-1), giving a 1% wt/wt concentration to the material. This mixture was continuously stirred for 12 hours and then filtered using a $0.22\,\mu m$ syringe filter [37]. In preparation for the photopolymerization process, a drop of the developed solution was placed on a hot plate, and was condensed at $50^{o}C$ for 90 minutes. This process triggers the silanols to react together to form a stiff, non-flowing siloxane network, due to the evaporation of the water content from the solution, leading to the formation of a gel with increased viscosity as shown in Fig. 2

1.3 Pyrolysis

Pyrolysis is a thermochemical decomposition process involving the heating of organic or polymeric materials in the absence of oxygen. Unlike combustion, which requires an oxidizing environment, pyrolysis causes bond breaking and molecular rearrangement in an inert or oxygen-limited environment [39]. During the pyrolysis process, the material undergoes several stages. Initial stages of heating involve the elimination of water and other volatile species. As the temperature continues to increase, the chemical bonds within the material start to break down, producing gaseous products and solid residue. The chemical breakdown causes the organic components of the material to decompose and evaporate, while the inorganic component starts to form dense networks. The final products of the pyrolysis process depend significantly on the processing parameters such as the temperature, heating rate, atmosphere and the precursor chemistry. Hence this makes pyrolysis an essential process for the fabrication of polymer-derived ceramics. The solid inorganic backbone left behind post pyrolysis, transforms into ceramics such as SiOC, SiC, SiCN which provide the exceptional material properties of typical ceramics that are exploited in various domains of science and technology.

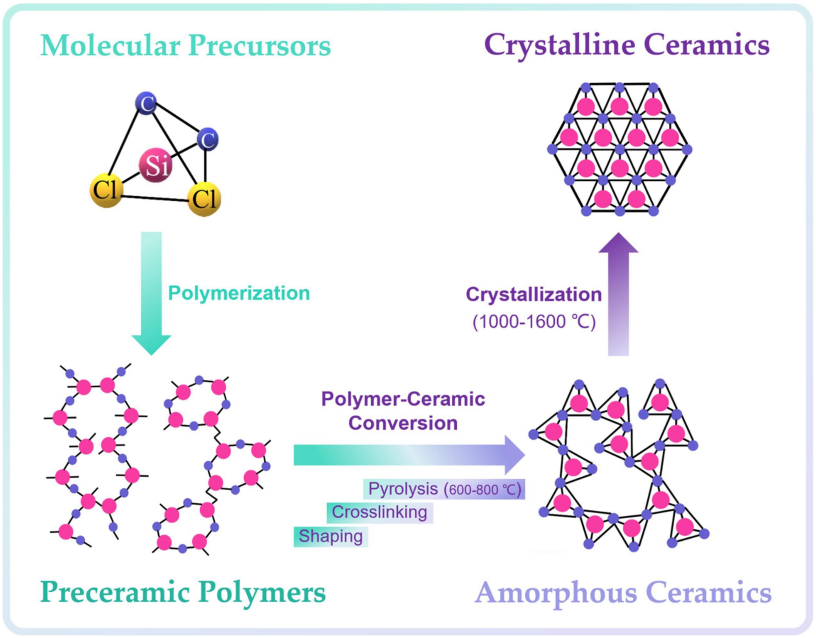

Figure 3: Schematic diagram indicating the conversion process of preceramic precursors to crystalline ceramics. Reproduced from [40]

One of the major consequences of pyrolysis is material shrinkage. As the organic groups are eliminated and the inorganic component densifies, the fabricated structures decrease in volume, causing significant mass loss and shrinkage in the structures. This shrinkage can be beneficial, as it provides increased density and reduced feature sizes in the fabricated structures, however it can also introduce defects such as cracks or pores if the heating rate is too high, or if the volatile components are unable to escape efficiently. Therefore, careful control of the pyrolysis parameters is essential, and hence slow heating of the structures

is often preferred to allow gradual decomposition of the microstructures, reducing internal stress and providing improved structural integrity. Along with introduction of defects, another effect that is commonly observed during heat treatment of polymerized structures is delamination, where the structures detach from the substrate due to the material shrinkage during pyrolysis. Detachment of the fabricated structures is a direct consequence of the observed material shrinkage and it is also strongly affected by the chosen temperature ramp and the selected constant heating temperature. Along with that, the chosen atmosphere during pyrolysis also plays a significant role. Oxidation is prevented when an inert atmosphere such as nitrogen or argon is used, allowing the carbon containing ceramic structures to be retained. In contrast pyrolysis in air (often termed as calcination) can lead to oxidation, removal of the carbon, or the formation of oxide ceramics. Hence the choice of atmosphere directly affects the composition, porosity and the mechanical properties of the final product obtained post pyrolysis.

1.4 Two-Photon Polymerization

Two-Photon Polymerization (TPP) [9] is a laser direct writing technique based on nonlinear light-matter interactions induced by tightly focused lasers of femtosecond duration. Here due to the nonlinear effect, the polymerization process is confined only to the laser focus spot, through the simultaneous absorption of two photons by the photoinitiator. Unlike the conventional UV photolithography, which relies on one photon absorption by polymerizing the entire path of light passing through the photoresist, TPP exploits nonlinear optics to achieve very high spatial confinement of the polymerization reaction. It results in the fabrication of truly free-form 3D structures with sub-micrometer to nanometer scale resolution. This high spatial confinement is achieved using a focusing objective with high numerical aperture (NA). The spatial resolution of the focused laser beam is dependent on the wavelength of light and the numerical aperture of the objective, and this relation is quantified as the Rayleigh Criterion:

$$r = \frac{0.61\lambda}{NA} \tag{7}$$

Where r is the radius of the Airy Disk formed, λ is the wavelength of light, and NA is the numerical aperture of the lens. Although the focused laser spot and hence the resolution of the printed structures is fundamentally limited by diffraction, the effective polymerized volume is further influenced by various other factors of multiphoton absorption. The commonly used resins employed as prepolymer/photosensitive resins are designed to be sensitive to UV but transparent to most visible and infrared radiation. During photolithography using UV, single photon absorption occurs, where each photon incident on the photoresist has sufficient energy to excite the molecules of the resin from the ground state to an excited state. Hence the absorption rate scales linearly with intensity, resulting in exposure along the entire path

of the beam in accordance to Beer's Law (Eq. 9).

$$Rate \propto Intensity \tag{8}$$

$$I = I_0 e^{-\alpha z} \tag{9}$$

Here, I_0 indicates the initial intensity, α is the linear absorption coefficient, and z is the penetration depth. As the light passes through the resin, it polymerizes the entire path through the resin, hence the cross-linking density of the negative tone resists decreases exponentially with increasing penetration depth. This applies limits to the fabrication of complex and truly arbitrary 3D structures with high resolution. In order to overcome such limitations, we introduce nonlinearity in the system. Optical nonlinearity is introduced when instead of absorbing a single photon (1PA), two or more photons are simultaneously absorbed (2PA, 3PA, etc) Fig. 4. In order for the resin to absorb two (or more) photons simultaneously and trigger the nonlinearity of the system, the intensity of the laser beam must be very high. This high intensity is achieved by high temporal confinement, employing ultrashort laser pulses of femtosecond duration. Such short laser pulses provide the necessary intensity for the nonlinear two-photon absorption to occur in the photoresist. This nonlinearity generalizes the relation in Eq. 8:

$$Rate \propto Intensity^n \tag{10}$$

Where n represents the order of nonlinearity. For $n = 1$, we obtain the single photon absorption (Eq(8)). As the order of nonlinearity increases, the rate of absorption scales nonlinearly with the intensity of the laser pulses. Hence absorption of the photon only takes place at those places in the resist where the intensity is high enough to the power of n, implying that the polymerization reaction is now confined to the focus spot of the laser, as the intensity profile decays smoothly around the focus spot. This causes localized chemical reaction in the resist as mentioned earlier, hence providing the freedom to fabricate complex 3D structures by scanning the laser across the surface of the resist, while simultaneously providing high resolution by high spatial confinement.

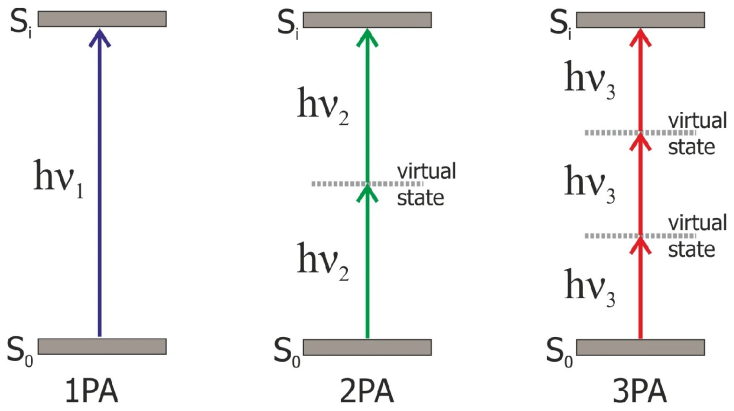

Figure 4: 1PA, 2PA and 3PA, reproduced from [41]

1.5 Voxel Polymerization and Threshold Behavior

The smallest element that can be polymerized in the photoresist is termed as the volumetric pixel, or simply 'Voxel', which serves as the fundamental building block of all printed structures [42]. While the voxel size is fundamentally limited by diffraction, it is also strongly governed by the polymerization threshold, which is the minimum amount of local energy dose that needs to be supplied to the photoresist in order to polymerize the resin at the exposed volume, so that it can form long polymer chains and survive the development process. Thus even though multiphoton absorption (MPA) is a probabilistic phenomenon, the material response to the nonlinearity is ultimately a threshold limited behavior.

Due to the Gaussian intensity profile of the focused laser beam, the voxel exhibits an ellipsoidal shape, with maximum intensity at the center, which smoothly decays towards the periphery. Since polymerization occurs only at regions where the local intensity exceeds the threshold, the cross-linking of the polymer chains occurs only at the center as the intensity falls below the threshold at the periphery. Thus providing smaller features for the printed structures. Therefore when the threshold is high relative to the applied intensity, polymerization is confined to the central region of the focus, resulting in smaller voxels and higher resolution. Conversely, excessive laser intensity leads to voxel broadening and may approach the optical damage threshold of the material. This relationship between the voxel and the laser intensity is shown in Fig. 5.

The range of exposure conditions that allow controlled polymerization without damage, which is defined by the laser power, scanning speed, repetition rate, and material response, is referred to as the fabrication window. Importantly, this fabrication window does not stay constant for a given material, i.e. it is not static but dynamic, as it depends on processing conditions. Variations in the scanning speed alter the effective local dose, while high repetition rates or low scanning speeds can lead to heat accumulation. Insufficient heat dissipation promotes radical diffusion beyond the focal volume, resulting in unintended polymerization, increased feature sizes, and reduced resolution. Changes in the laser scanning speed directly

affects the threshold behavior of the material. For a fixed laser power, variations in the scanning speed changes the local energy dose supplied to the photoresist. Thus increasing the speed too high may reduce the intensity below the threshold, while decreasing it may lead to overpolymerization, due to excessive localized energy dose provided to the material. Additionally, heat accumulation also plays a major role in the dynamic nature of the fabrication window. High repetition rate pulsed lasers or low scanning speeds do not allow the heat to dissipate efficiently from the polymerized focal spot. This accumulated heat energy promotes radical mobility, allowing the radicals to propagate away from the exposed focal spot and polymerize around it, thus unintentionally increasing the feature size and reducing the resolution of the printed structures. Thus accurate recreation of the intended geometries requires careful balancing of the correct laser parameters, to work within the dynamic fabrication window of the resist.

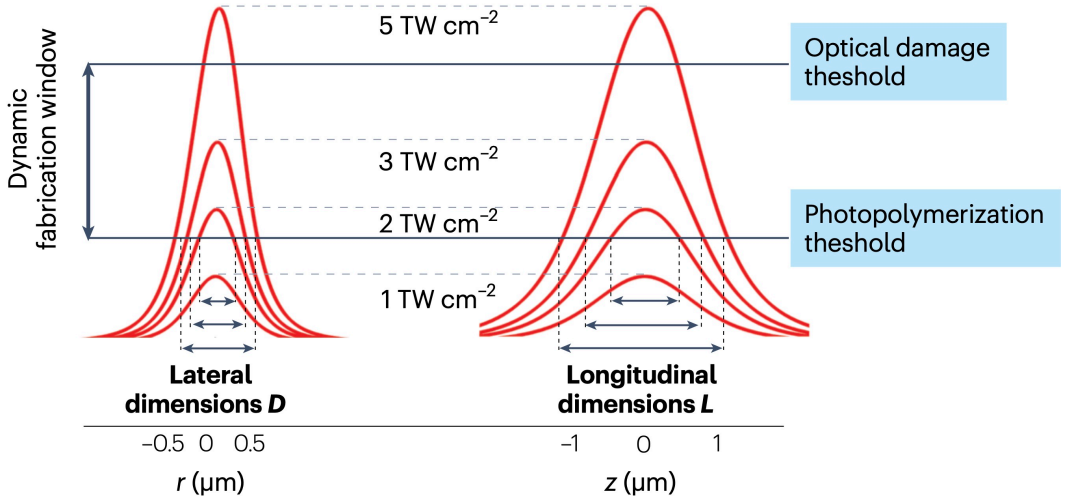

Figure 5: Dependence of the dimensions of the polymerized segment (voxel) on the intensity of the exposed laser beam in the focal plane and the thresholds of polymerization and polymer optical damage [43]

1.6 3D Micro-Optics

Microoptics is a branch of optics concerned with the design, fabrication and characterization of optical components with dimensions in the micrometer range. Governed by the same fundamental rules of electromagnetic theory as conventional optics, optical systems at the microscale exhibit significantly stronger diffractive effects due to their dimensions approaching the wavelength of light, making it essential to consider the effects of wave optics. Such micro-optical components are now widely integrated into compact optical systems where conventional bulk optical components become impractical due to size limitations [44].

Due to the strong confinement and high resolution achieved during the polymerization process, TPP is particularly suitable for manufacturing optical elements with intricate three-dimensional geometries that are difficult to realize using other lithographic techniques.

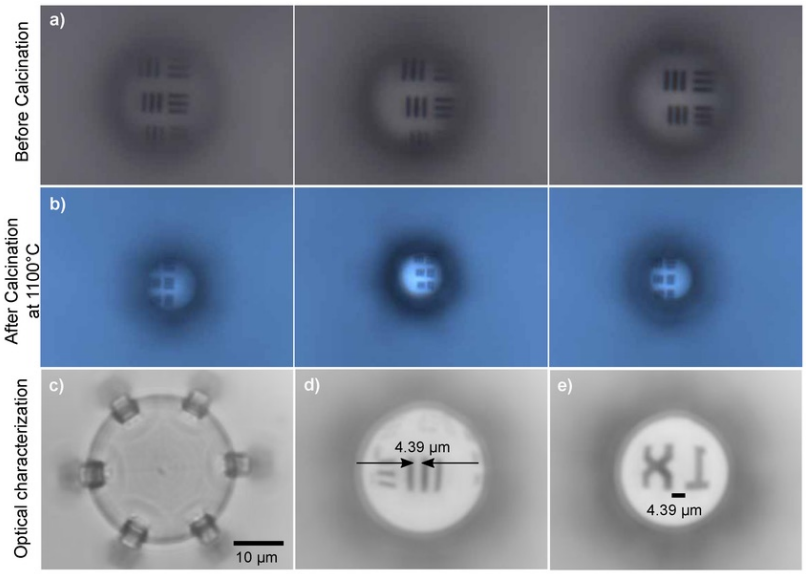

Figure 6: Optical images of microlenses before and after calcination, along with their characterization. Reproduced from [45]

Commonly fabricated micro-optical elements include microlenses [4], diffractive optical elements [46], waveguides, optical resonators and micro-prisms. Among these components, microlenses represent one of the most widely studied and fabricated structures in the realm of microoptics. They are often used for focusing, collecting and coupling light into other optical elements at the microscale. Diffractive optical elements (DOEs) constitute another important class of micro-optical components. Unlike microlenses which manipulate light through curved surfaces and refractive index modulation, DOEs use nanoscale phase modulation to shape wavefronts. Since the performance of all these components strongly depends upon efficient transmission of light and precise wave control, the majority of the micro-optical elements are fabricated using highly transparent materials. Transparency minimizes absorption and scattering losses, thereby preserving the optical properties of the system. As a result, most micro-optical elements fabricated using two-photon polymerization are polymeric and optically transparent in nature [47]

1.7 Opaque Microstructures

Although two-photon lithography is mostly employed for the fabrication of transparent optical components, which are designed using transparent polymers, this inherently creates a design limitation for the integration of absorptive or opaque components within microscale systems. In practical systems, the manipulation of light is not only limited to effective transmission, but it also requires suppression, filtering and absorption of unwanted or stray light, which inherently improves the transmission and manipulation of the light passing through the optical setup at the microscale. The absorptive components include apertures, beam stops, beam blockers, stray light filters, optical isolators and microscale masks. Such absorptive optical elements remain relatively unexplored in the realm of additive manufacturing using

laser direct writing techniques. The reason for this is that the opaque resins required for the fabrication of such structures strongly absorb light from the UV to the near-infrared regime. This prevents sufficient light penetration into the resin required for photopolymerization, which shows that achieving opacity in structures fabricated using two-photon polymerization systems is inherently challenging due to strong reliance on transparent photoresists for efficient nonlinear absorption. The limited exploration of opaque microstructures that has been conducted in the recent years has shown two different methods of fabricating opaque or 'black' structures. One of the demonstrated ways is the controlled overexposure of the laser, causing uncontrollable 'burning' or carbonization of the resin, leading to randomized or irregular formation of such 'black' structures [17] Fig. 7(a,b,c,d). Another successful method of fabricating opaque structures employs the use of commercially available opaque organic photoresist IP-Black [48], Fig. 7(e,f,g,h). However the opaque microstructures obtained post fabrication are organic in nature, which have low damage thresholds, low hardness and reduced chemical stability, which are all essential properties required for optical components with high absorptivity. In this study, we aim to overcome these limitations by using a novel transparent hybrid inorganic-organic resin for the fabrication of high resolution microstructures using two-photon polymerization, which turn completely opaque and inorganic post pyrolysis .

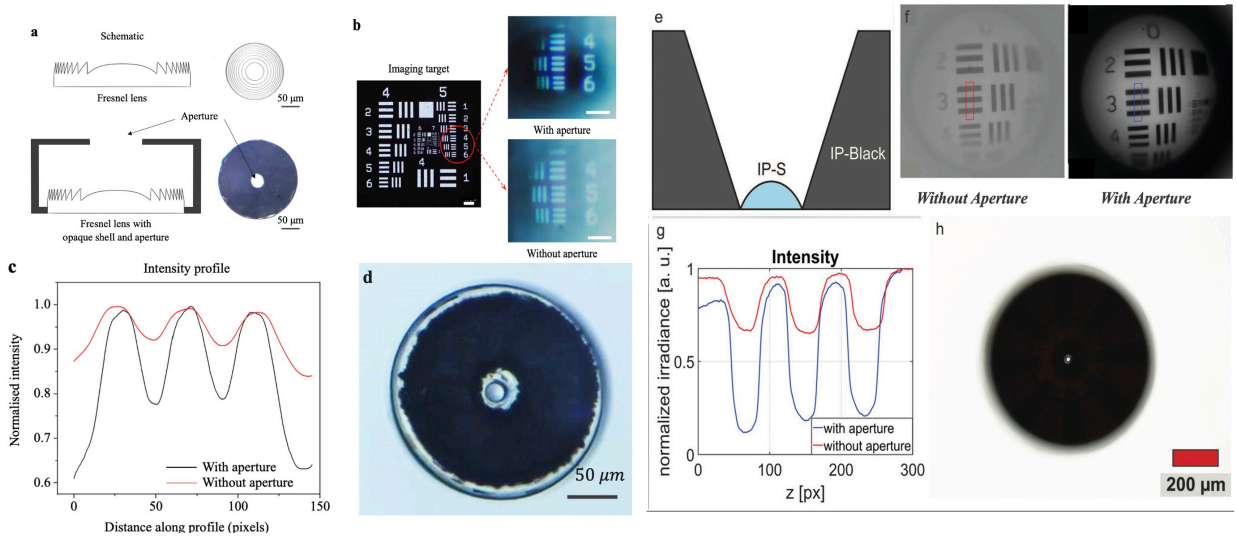

Figure 7: Opaque structures obtained using laser overexposure, showcasing the applications of the opaque apertures for stray light suppression and improving image contrast (a,b,c,d) [17]. Opaque structures obtained using organic resist IP-Black, indicating similar applications for stray light suppression (e,f,g,h) [48]

2 Experimental Methods

2.1 Laser Direct Writing

The laser setup used for the fabrication process was the home-built Laser FemtoLab setup Fig. 8. The system consists of a pulsed laser source operating at the central wavelength of $\lambda_c = 1030\,nm$, with a pulse duration of $\tau < 300\,fs$, and a repetition rate of $f = 200\,kHz$. The system can also be used in the second harmonic wavelength of $\lambda_{SH} = 515\,nm$, which was the wavelength chosen for the experiments. The laser setup consists of two different positioning stages, consisting of a XYZ translation stage for the sample, and a second positioning stage for the laser, labeled as AB. Finally, in order to focus the laser beam onto the resin to a diffraction limited spot, a Plan Apochromat Zeiss 20x dry objective with $NA = 0.8$ was used.

The laser setup is controlled by a software which is divided into two parts, namely 3DPoli Compiler and 3DPoli Fabrication respectively. 3DPoli Compiler is used for setting the geometries of the structures to be fabricated. It allows complete control over the 3D geometry and compilation of the code written for the construction of the structures. The code written for the construction of the structures includes all the information about the various parameters, such as the translational and laser positioning stages, (XYZ and AB respectively), scanning speed of the laser, the power used for fabrication, the opening and closing of the laser shutter, etc. On the other hand, 3DPoli Fabrication provides hands-on access to the actual fabrication process, by granting the user manual control over the changing position of the translation stages, laser intensity values, laser power calibration etc.

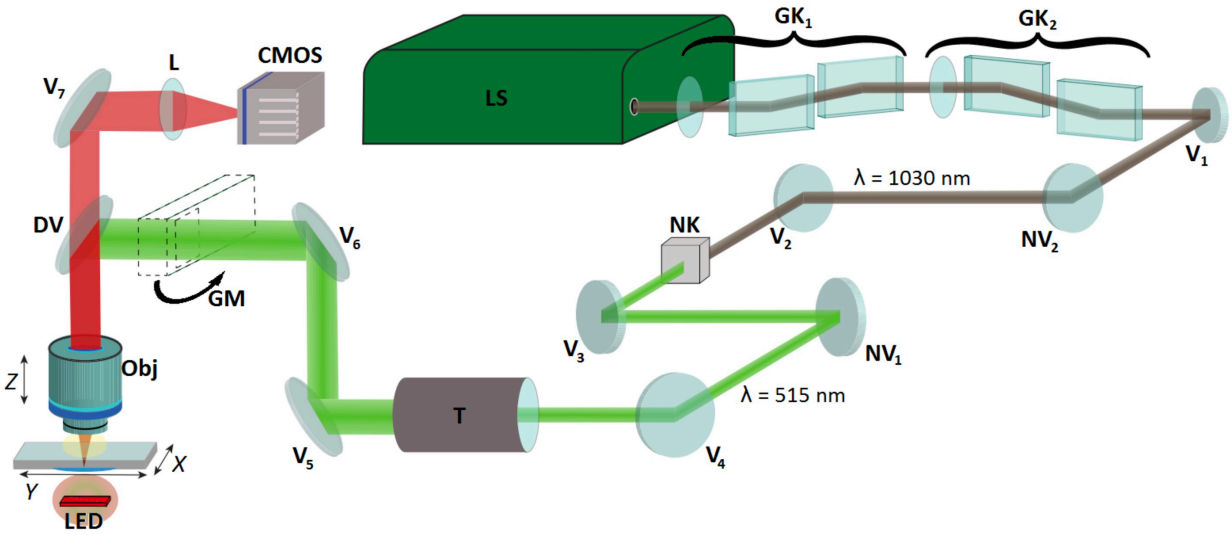

Figure 8: Schematic representation of the FemtoLab setup. LS- Pharos (Light Conversion), $\lambda_c = 1030\,nm$, $f = 200kHz$, $\tau < 300\,fs$, GK_1, GK_2-power adjusters, NV_1, NV_2-detachable mirrors,$V_1 - V_6$-Mirrors, NK-Nonlinear crystal, T-Telescope, GM-Galvanometric Scanner, Obj-20x, NA=0.8, CMOS-Camera. Reproduced from [49]

The fabrication process was performed from the 'Top to Bottom' approach, whereby the resin was placed facing away from the laser, allowing the laser light to pass through the substrate into the resin, printing the structures upside-down. This was done in order to avoid any aberrations that might occur to the laser light due to the curved shape of the droplet. Hence, the substrate is placed onto the XY translation stage with the droplet facing away from the laser, and the objective lens is fit onto the setup. The objective is then lowered manually by changing the Z axis until we find that the laser focus spot is located precisely at the substrate-resin interface. This is an essential step in order to ensure that the fabricated structures are printed onto the substrate, and are not printing above, or inside the substrate. The interface is then identified by selecting a suitable laser power, followed by printing of voxels. The Z axis is altered depending upon the size of the voxel observed, until the polymerization is barely visible. This indicates that we have now arrived at the substrate-polymer interface.

After the stages are set at a desired location, the code is compiled and then sent for fabrication. After the fabrication process is complete, the sample is removed from the stage and the process proceeds to the next stage, that is the development of the polymerized structures.

2.2 Development

The development procedure enables us to extract the fabricated structures from the polymer droplet. The process involves immersing the sample in a specific developer solution, which dissolves the unexposed regions of the resin. Since this resin is a negative-tone resist, the solubility of the cross-linked polymer chains decreases on laser exposure, thus the developer solution dissolves away the unexposed regions, leaving the cross-linked polymerized structures on the substrate. Thus it is important to find the substrate-polymer interface correctly, so that the structures remain attached to the substrate and are not washed away by the developer solution. In this study, the sample was immersed in methyl-isobutyl-ketone for 60 minutes, and then removed from the solution and allowed to dry for 5 minutes Fig. 9

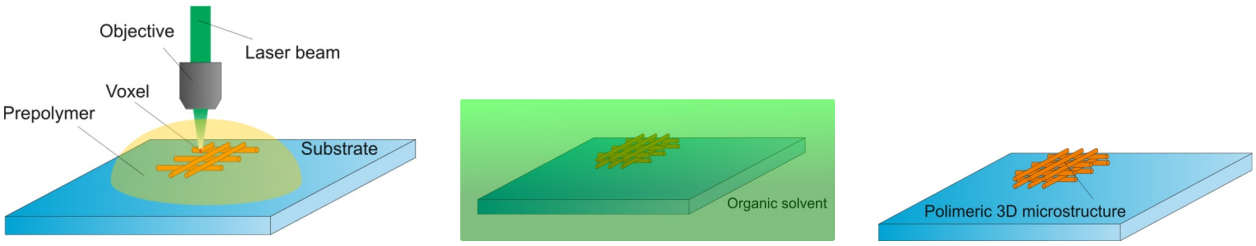

(a) Laser direct writing into the polymer droplet

(b) Removal of uncured resin in chemical bath

(c) Final product obtained post fabrication and development

Figure 9: Schematic diagram showing the fabrication and development process to obtain the polymerized microstructures. Reproduced from [50]

2.3 Characterization

Before the post processing of the structures was performed in order to remove the organic content of geometries via heat treatment, some preliminary characterization measurements were taken in order to observe and identify the outcome of the laser parameters used for fabrication of the structures. These characterization steps included simply observing the structures in an optical microscope after the development, or to observe the surface roughness of the successfully fabricated structures in the optical profilometer, to assess the smoothness of the fabricated structures. These initial characterization steps were repeated extensively during this study in order to identify the right laser parameters necessary for fabrication using this hybrid resin. After the initial characterization steps had ensured that the chosen laser parameters are sufficient for the intended geometries, then we can proceed to next step of post processing, which involves pyrolysis of the polymerized structures.

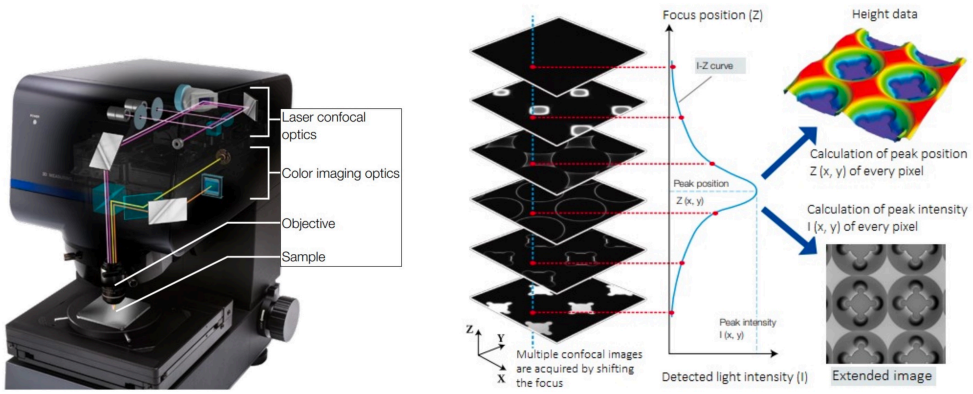

Figure 10: (a) LEXTTM OLS5100 3D Laser Scanning Microscope. (b) Height measurement principle. Re-produced from manufacturer's manual [51].

- **(i) Optical Profilometer:** The LEXTTM OLS5100 3D Laser Scanning Microscope has two optical systems (color imaging and laser confocal) as shown in Fig. 10 which allow the acquisition of shape information of the printed structures, along with high quality images. The confocal system was used in this study to observe the nature of the surface post-fabrication and post pyrolysis. This system consists of a 405 nm laser diode which acts as the light source and a photomultiplier as detector, which receives the light focused through a circular pinhole instead of all the light reflected and scattered from the sample, which helps acquire images with higher contrast than with an ordinary microscope. The microscope automatically adjusts the focus position to capture several confocal images in order to assess height, and provides 3D shape information of the sample's surface, providing accurate information regarding the average surface roughness of the fabricated structures and the structures post pyrolysis.

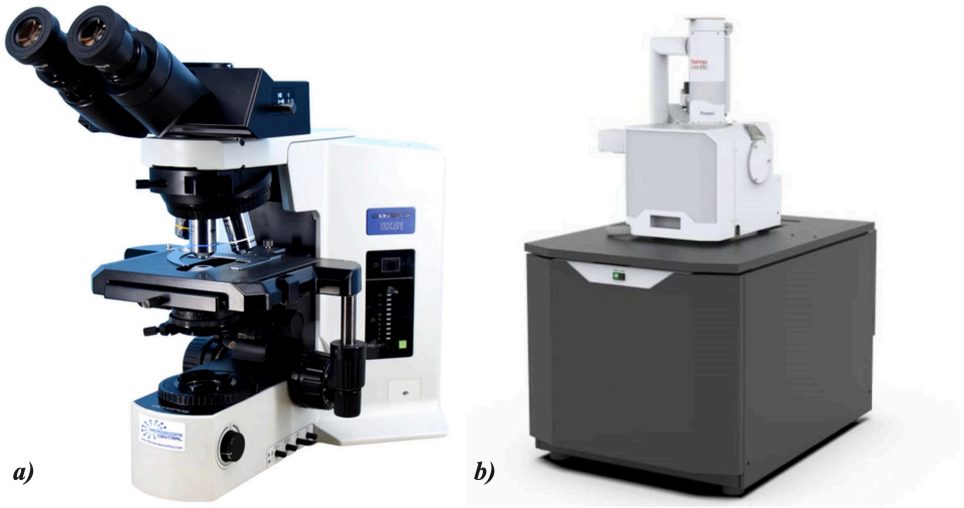

Figure 11: a) Olympus BX51 Optical Microscope along with the schematic diagram of the microscope, reproduced from the manufacturer's manual [52]. b) Scanning Electron Microscope, reproduced from the manufacturer's manual [53]

- **(ii) Optical Microscope:** The optical microscope Olympus BX51 shown in Fig. 11a was used to observe the sample in transmission, i.e. the sample was illuminated and observed from opposite sides, allowing the incident light to be transmitted through the structures and be observed by a camera on the other side. The magnifications offered by the microscope are: 4x, 10x, 20x, 40x. It is important to note that the aim of observation under the optical microscope is not to obtain a high resolution image of the structures, but instead to observe and detect any major defects or damages that may have occurred during the fabrication or the development stages.

- **(iii) Scanning Electron Microscope (SEM):** After the structures undergo the high temperatures treatment to eliminate the organics from the polymerized structures, the substrate was observed under the Scanning Electron Microscope (SEM) to accurately assess the dimensions of the post pyrolysis structures. The Scanning Electron Microscope (SEM) used in this study for characterization of the structures is the Thermo Fisher Scientific's model Prisma E (Fig. 11b). The SEM uses a highly focused beam of energetic electrons that are incident on the surface of the structures fabricated on the substrate, in order to study the surface morphology and obtain high resolution images of the structures. This is possible because unlike optical microscopes, which use mirrors and lenses along the direction of propagation of light in the visible spectrum to obtain images, the SEM uses electrons, which have significantly smaller wavelength than visible light, allowing it to achieve high spatial resolution, often down to the nanometer scale. Before inserting the sample in the SEM, it is necessary to coat them with a thin layer of conducting metal. This is done in order to avoid any kind of charge accumulation of the non-conducting polymerized structures, which may lead to damaging the structures. Throughout this work, all the structures were sputtered with 10 nm layer of silver.

2.4 Pyrolysis

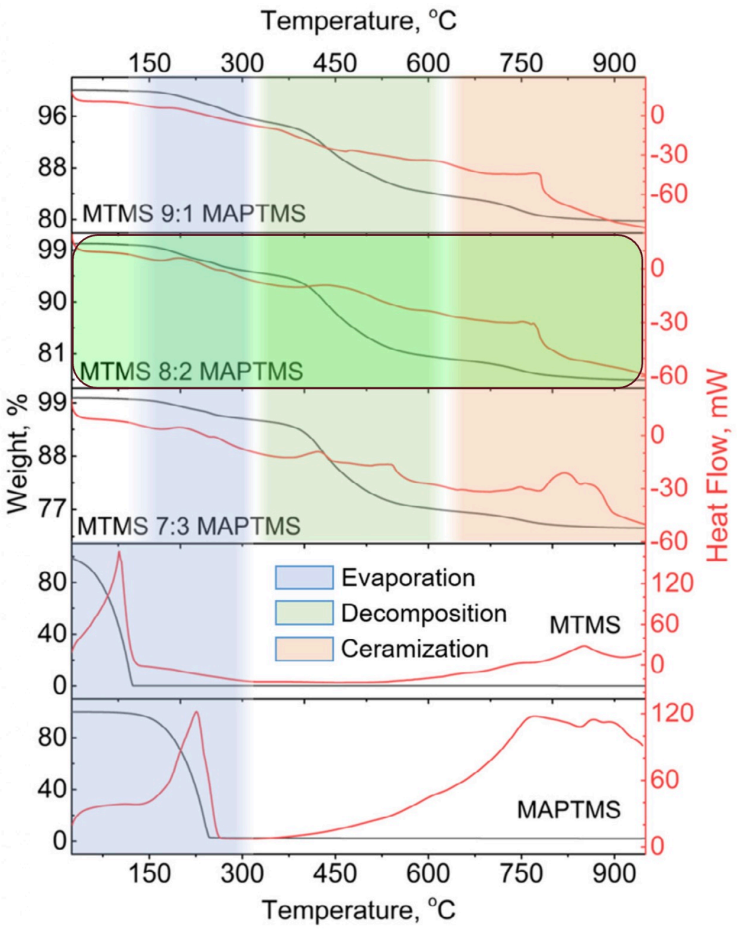

Figure 12: Thermogravimetric Analysis of MTMS:MAPTMS (8:2) (highlighted in green) for polymers and initial precursors showing the weight loss (black curve) and heat loss (red curve) as a function of temperature. Reproduced from [37])

Due to the hybrid nature of the resin, the polymerized structures have to undergo heat treatment in order to obtain truly inorganic 3D microstructures. Pyrolysis of the structures was realized at 1000^oC for 1 hour in an inert nitrogen atmosphere, with an initial temperature ramp of $5^oC/min$, which was later decreased to $1^oC/min$. Decreasing the temperature ramp to $1^oC/min$ significantly increases the processing time, however, this rate is essential for the chosen geometry of this study, where the slow and gradual increase in temperature allows for efficient elimination of volatile organic species, reducing the development of internal stress within the structures, and preventing delamination of the fabricated structures, a common phenomenon observed during thermal treatments of polymerized components. It is also important to note that the substrate should be chosen such that it can survive extreme heat treatment without being damaged. Quartz substrates were used in this study for the pyrolysis process due to their suitable temperature properties. During the annealing process, initially temperatures around $100 - 300^oC$ mark the dehydration process (Fig . 12), characterized by the removal of water content from the polymerized structure. The geometries do not experience significant mass loss during this process, and hence the overall shape of the structure is still retained. The next step is the organic pyrolysis, which occurs

at a temperature range of $300 - 600^oC$, where the volatile organic solvents present in the structures start to decompose, leading to significant mass loss, followed by shrinkage of the structures. The shrinkage can also lead to the formation of air bubbles in the structure if the volatile gases are not allowed to escape gradually and efficiently. These air bubbles can be tremendously problematic for applications in optical elements, since the presence of air bubbles can alter the local refractive index of the material. Finally, the last step includes the inorganic consolidation, which occurs at temperatures greater than 800^oC. The major structural transformation of the inorganic geometries occurs in this stage of the pyrolysis, whereby the structures truly densify, and the final bond structure, mechanical properties and refractive indices are obtained.

2.5 Transmission

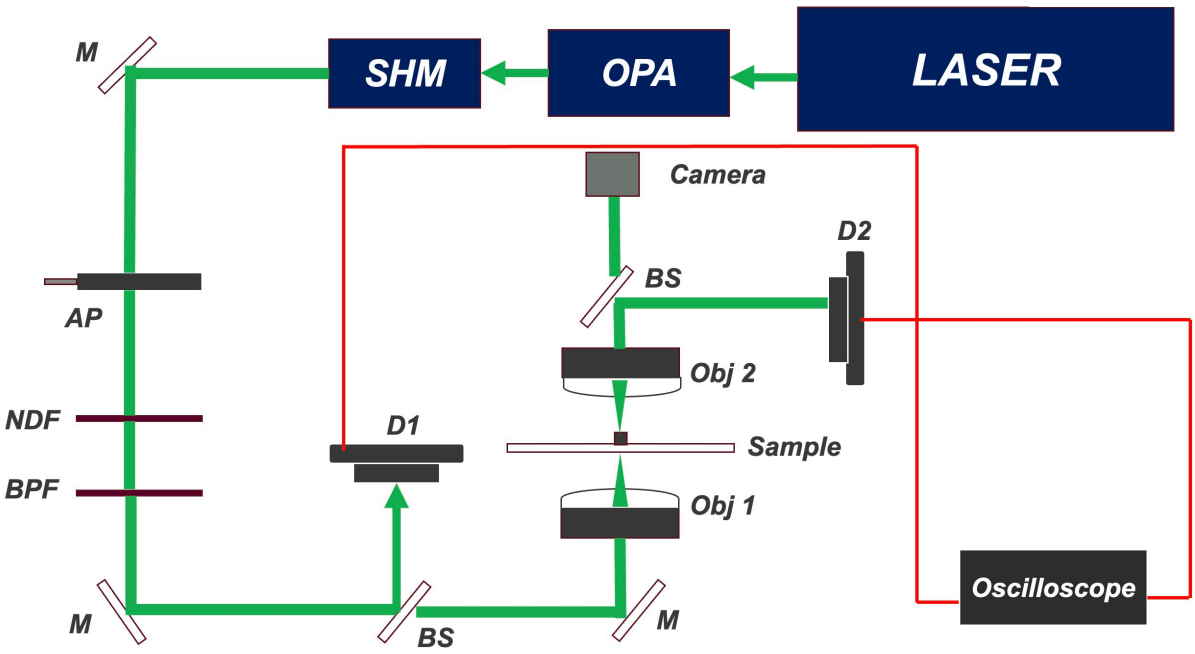

Figure 13: Schematic representation of the transmission measurement setup. Laser- Pharos (Light Conversion), $\lambda_{las} = 1030\,nm$, $\tau_{pul} = 300\,fs$, OPA-Optical Parametric Amplifier, Orpheus (Light Conversion), SHM-Second Harmonic Module, pulse tunability from $300\,nm - 2700\,nm$ Lyra (Light Conversion), M-Mirror, AP-Aperture, NDF-Natural Density Filter, BPF-Band Pass Filter, BS-Beam Splitter, D1,D2-Photodiodes, Obj1-20x, NA=0.4, 0bj2-10x, NA=0.25 [**?**]

The setup shown in Fig . 13 was used to characterize the fabricated microstructures after pyrolysis and evaluate their optical transmission. The laser beam generated by the source was first directed through an optical parametric amplifier (OPA) and a second harmonic module, in order to obtain the required operating wavelength for the transmission measurements. The chosen wavelengths for the measurements were $\lambda_1 = 633\,nm$ and $\lambda_2 = 510\,nm$. The beam was subsequently guided through a series of mirrors and filters in order to control the beam intensity, alignment and spectral purity before it reaches the sample. A beam splitter was

placed before the light was focused onto the sample, which diverted the beam onto the first photodiode, acting as the measurement for the reference beam. The second portion of the beam was allowed to be focused on the sample via objective 1, with the focus point being at the ceramic structures post pyrolysis, in order to evaluate their optical transmission properties. The light transmitted through the sample was collected by objective 2 above the sample. A second beam splitter redirected the transmitted beam towards the imaging camera, allowing real-time visualization of the beam spot and the alignment of the sample, while the other half of the beam was directed towards the second photodiode D2, which measured the signal transmitted through the fabricated structures. The two signals from the photodiodes were transmitted to the oscilloscope, and by comparing the signals obtained from the diodes, the transmission characteristics of the pyrolyzed structures were evaluated.

3 Experiments

3.1 Design Of 3D Solid Cuboidal Blocks

The design of one of the fabricated structures is shown in Fig. 14. The structures were solid cuboidal blocks, with its dimensions being 300x300x20 μm^3 in Fig. 14. Such solid cuboidal blocks were deliberately selected, as their relatively simple geometry enables the systematic realization of the fabrication process, the post-pyrolysis shrinkage, and most importantly, the optical transmission measurements, since the fully solid nature of the structures provides a continuous interaction volume, making them particularly suitable for the transmission measurements. Along with that, their straightforward geometry allows easier analysis of the vertical as well as lateral shrinkage observed post pyrolysis. The cuboidal blocks were fabricated with a constant hatching and slicing values of $\Delta H = \Delta Z = 0.35\,\mu m$. Hatching value determines the distance between the individual lines polymerized by the laser along the X and Y axes, while the slicing value determines the gap between each such fabricated lateral layers stacked along the Z axis. Both these parameters were initially taken to be $\Delta H = \Delta Z = 0.7\,\mu m$, but then experimentally determined to be 0.35 μm to ensure sufficient voxel overlap, ensuring the fabrication of truly solid cuboidal blocks.

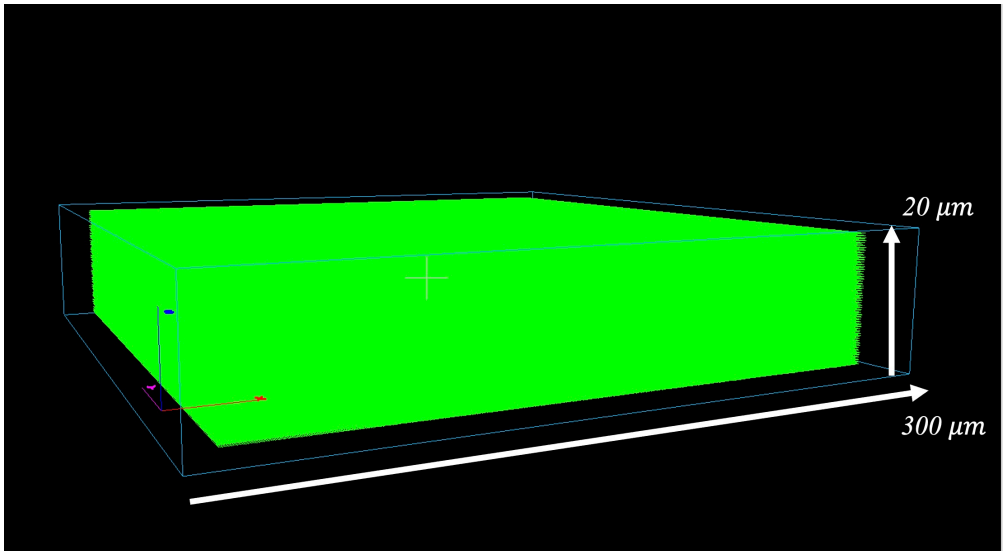

Figure 14: Design of the solid cuboidal block with vertical height $z = 20\ \mu m$ on the 3D Preview tab of the 3DPoli Compiler program

The large lateral dimension of 300 μm was deliberately selected to account for the shrinkage loss experienced during pyrolysis, and to ensure compatibility with the transmission measurements. Since the fabricated structures undergo significant volume reduction during pyrolysis, their initial dimensions were designed with respect to the laser beam spot size used for transmission characterization. Hence the cuboidal blocks were fabricated with a lateral size twice as large, to ensure that after shrinkage, their dimensions remain larger than the beam spot size, enabling accurate measurements and observation of light transmission through the opaque microstructures.

3.2 Finding Optimal Fabrication Parameters

The exposure dose plays an important role in the fabrication process, directly determining the degree of cross-linking and the feature sizes observed during the photopolymerization process. A correct balance of the exposure is essential in order to obtain structures that survive the development process and are fabricated without any cracks or deformations. Hence in order to identify the optimal fabrication parameters, a commonly applied methodology in two-photon polymerization was employed, which involved the fabrication of multiple cuboidal blocks arranged in a rectangular grid as shown in Fig. 15. The structures constructed in this grid were fabricated by varying the laser power along one of the grid axes from $P = 0.18 - 0.21$ mW in steps of $\Delta P = 0.01$ mW, and the laser scanning velocity along the other axes from $v = 1000 - 4000\,\mu m/s$ in steps of $\Delta v = 1000\,\mu m/s$.

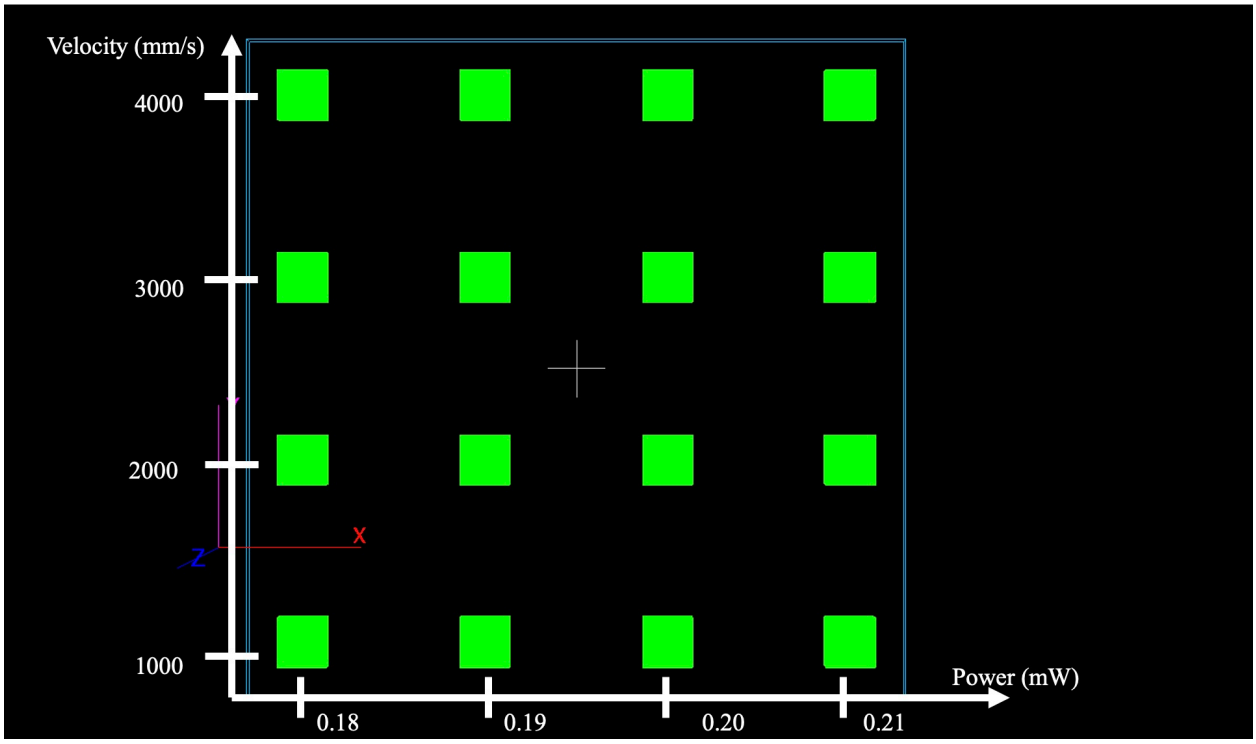

Figure 15: Design of the 300x300x20 μm^3 cuboidal blocks arranged in a rectangular grid, by varying the laser power along one axis and the scanning velocity along the other, as seen on the 3D Preview tab of the 3DPoli Compiler

3.3 Fabrication Of Cuboidal Blocks Of Varying Heights

After identifying the optimal parameters required for producing the solid cuboidal blocks, the next step involved fabricating structures with varying vertical heights. This was carried out in preparation for the transmission measurements aimed at investigating the dependence of optical transmission on the thickness of the opaque microstructures obtained post pyrolysis. By systematically varying the vertical heights of the structures, the effect of structural thickness on light transmission could be observed and evaluated.

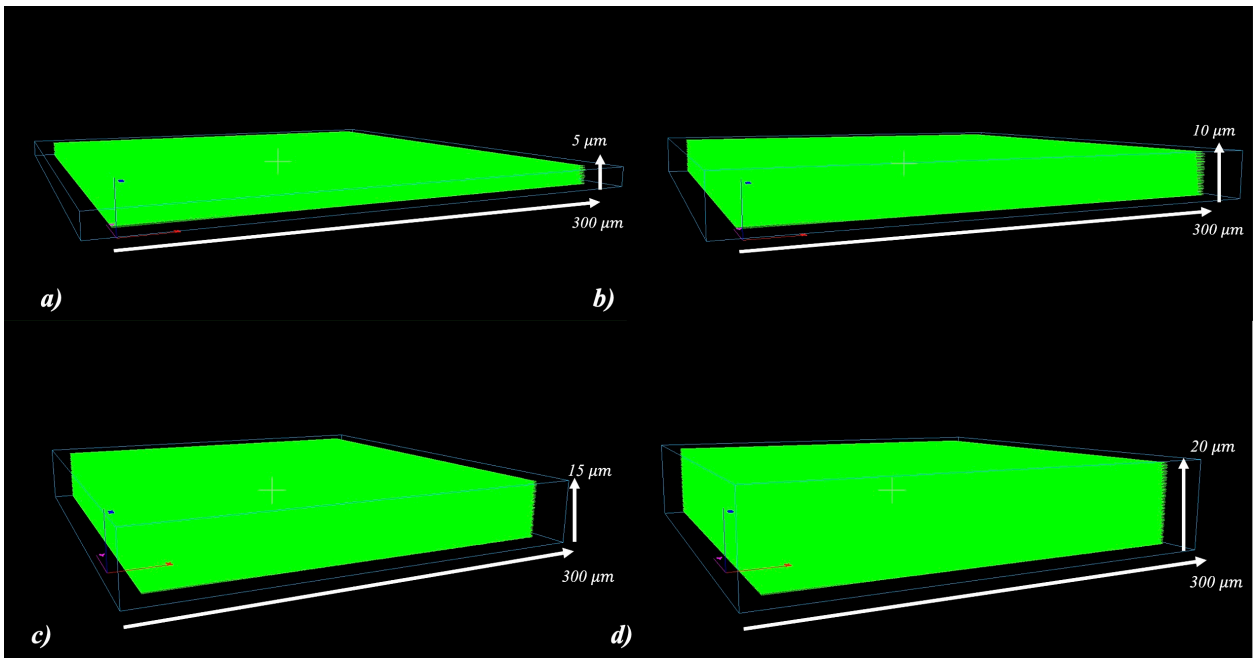

Figure 16: Design of the fabricated solid cuboidal blocks of vertical height $z = 5\,\mu m$ (a), $z = 10\,\mu m$ (b), $z = 15\,\mu m$ (c) and $z = 20\,\mu m$ (d), as seen on the 3D Preview tab of 3DPoli . (Fabricated with hatching and slicing parameters $\Delta H = \Delta Z = 0.35\,\mu m$)

3.4 Pyrolysis

Following the fabrication and development of the structures, the next step was to conduct pyrolysis experiments to investigate the ceramic conversion behavior of the microstructures, and evaluate their suitability as optically opaque components. The structures that underwent the thermal treatment were the fabricated cuboidal blocks of varying vertical heights from $z = 5\,\mu m$ to $z = 20\,\mu m$. It is important to highlight the importance of the chosen geometry of cuboidal blocks for pyrolysis, as the simplified geometry of the selected structures provides easier analysis of the volumetric shrinkage observed in the structure post pyrolysis. Since the blocks undergo significant mass loss and densification during the pyrolysis process, it was expected that the thicker structures would experience different thermal stresses and shrinkage behavior than the thinner ones. In particular, it was expected that the thicker structures would exhibit higher shrinkage than the shorter structure, due to presence of less restrictions on the vertical height of the taller structures, allowing higher shrinkage, while the shorter structures have reduced freedom of contraction in the vertical direction due to their adhesion to the substrate

3.5 Transmission Measurements

The transmission measurements were performed on the ceramic microstructures obtained post pyrolysis in order to analyze the opacity of the structures, and to study their interaction with visible light post pyrolysis. Since the structures are intended for future applications in microoptics, in the form of absorptive optical components as beam blockers, stray light filters and amplitude masks, it was essential to experimentally characterize their ability to suppress light transmission post high-temperature thermal treatment. Since the measurements were conducted on cuboidal blocks of gradually increasing vertical heights, the aim was to systematically increase the propagation length of the light through the interior of solid ceramic block, and observe its dependence of optical attenuation on the structure thickness. The transmission setup used in this study is shown in Fig. 13.

In addition to the measurements made by the photodiodes shown in Fig. 13, the imaging of the transmitted beam was also performed using a camera placed after the sample. These images were analyzed by generating intensity distribution heat maps using MATLAB. The heat maps provided qualitative data on the transmitted beam profile, which was too weak to be visible on the image captured by the camera. Combining the quantitative data extracted from the photodiodes and analyzed by the oscilloscope, along with the qualitative data obtained from the camera image after processing them in MATLAB, the overall investigation provided a more comprehensive characterization of the optical behavior of the fabricated microstructures.

4 Results and Discussion

4.1 Realization of The Solid Cuboidal Blocks

The initial set of fabrication experiments consisted of a preliminary laser power sweep aimed at identifying the minimum power required to produce mechanically stable solid cuboidal blocks. Hence the blocks were fabricated by varying the laser power from $P = 0.12$ mW to $P = 0.15$ mW while maintaining a constant laser scanning velocity of $v = 1$ mm/s and a fixed structural height of $z = 20\ \mu m$. All the structures were fabricated on borosilicate glass substrates using hatching and slicing parameters of $\Delta H = \Delta Z = 0.7\ \mu m$. The fabricated structures obtained using the preliminary power sweep are shown in Fig. 17

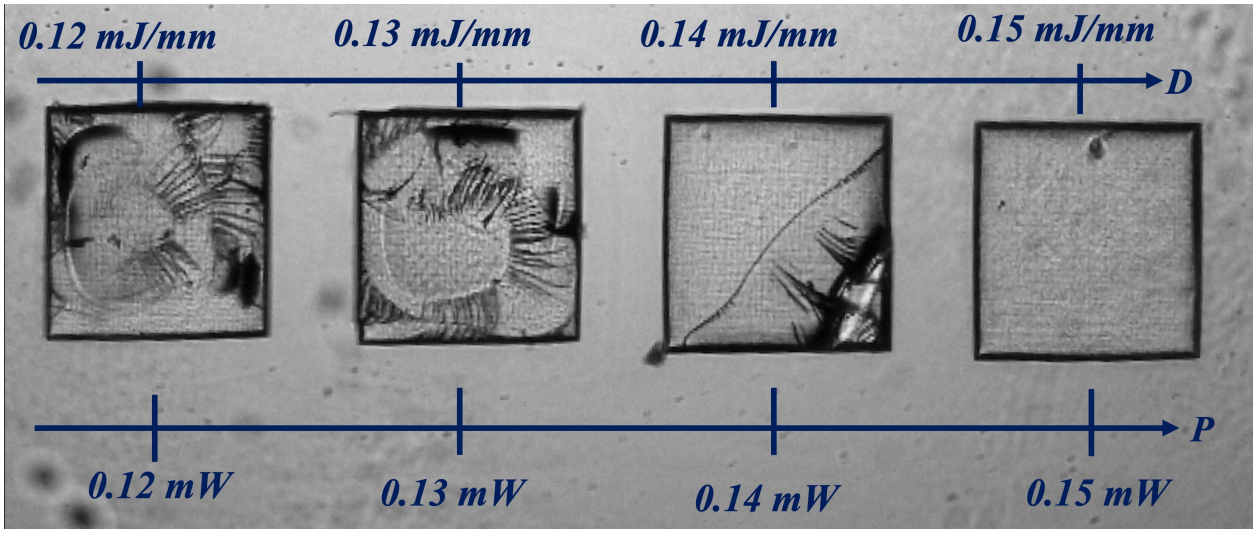

Figure 17: Optical microscope image of the preliminary power sweep showing the fabrication of solid cuboidal blocks of height $z = 20\ \mu m$ and velocity $v = 1$ mm/s. The hatching and slicing parameters for all the structures were $\Delta H = \Delta Z = 0.7\ \mu m$

As evident from Fig. 17, the laser power of $P = 0.15$ mW produced the highest quality structures. The lower laser powers used for the preceding structures provided insufficient dose to the resin, resulting in incomplete cross-linking and consequently leading to cracked and deformed cuboidal blocks with poor structural integrity after development. Since the preliminary power sweep was conducted only for a fixed vertical height of $z = 20\ \mu m$, the next step was to evaluate if the selected laser parameters remained suitable for structures with larger vertical heights. To investigate this, a second set of structures were fabricated with sequentially increased heights ranging from $z = 20\ \mu m$ to $z = 60\ \mu m$, while maintaining the previously optimized laser parameters of $P = 0.15$ mW and $v = 1$ mm/s. The resulting structures are shown in Fig. 18

Fig. 18 shows that the structures continued to exhibit cracks and structural deformations despite being fabricated using the optimal laser power of $P = 0.15$ mW. Notably, even the cuboidal structure with the smallest vertical height of $z = 20\ \mu m$ displayed signs of internal damage. A plausible explanation for this behavior is insufficient voxel overlap within the

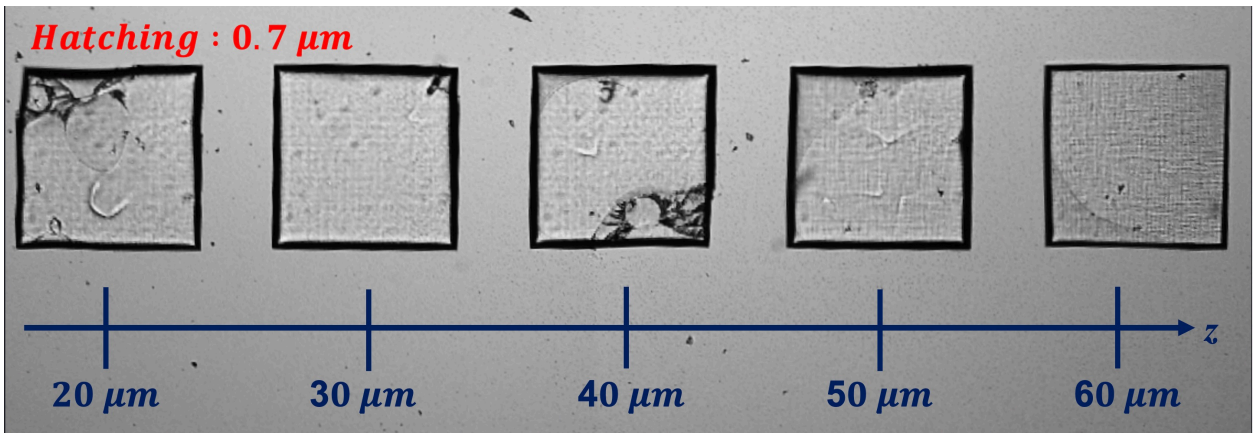

Figure 18: Optical microscope image of polymerized solid cuboidal blocks of varying vertical height from $z = 20 - 60\ \mu m$, with hatching and slicing parameters $\Delta H = \Delta Z = 0.7\ \mu m$. These structures were fabricated with laser power $P = 0.15$ mW and scanning velocity $v = 1$ mm/s

fabricated structures. When the structures were fabricated using the hatching and slicing parameters of $\Delta H = 0.7\ \mu m$ and $\Delta Z = 0.7\ \mu m$ respectively, the spacing between the adjacent voxels may be too large to achieve complete cross-linking throughout the structure. This could result in the formation of gaps or weakly polymerized regions within the structure, allowing the developing solvent to penetrate into the interior of the structures during development, leading to cracks and deformation.

Using Eq (7), along with the laser wavelength of the setup $\lambda = 515$ nm, and the numerical aperture of the objective used (NA = 0.8), we can estimate the theoretical value of the voxel radius as:

$$r_{theo} = \frac{0.61 \times 515 \times 10^{-9}}{0.8} = 393\,nm \tag{11}$$

Thus the diameter of the voxel is:

$$d_{theo} = 2 \times r_{theo} = 785\,nm \tag{12}$$

Thus Eq (12) suggests that the estimated voxel diameter is comparable to the selected hatching and slicing distances of $\Delta H = \Delta Z = 0.7\,\mu m$. This suggests that the overlap between adjacent voxels may be insufficient to ensure continuous cross-linking throughout the polymerized structures. As a result, weakly polymerized regions may allow the developing solvent to penetrate inside the structure, damaging the mechanical integrity of the solid cuboidal blocks.

To investigate this, the structures were fabricated again using the same laser power and scanning velocity of $P = 0.15$ mW and $v = 1$ mm/s respectively, while reducing the hatching and slicing distances by half to $\Delta H = \Delta Z = 0.35\ \mu m$. These values were reduced to improve the voxel overlap and significantly decrease the spacing between adjacent voxels. The structures obtained by reducing the hatching and slicing values are shown in Fig. 19

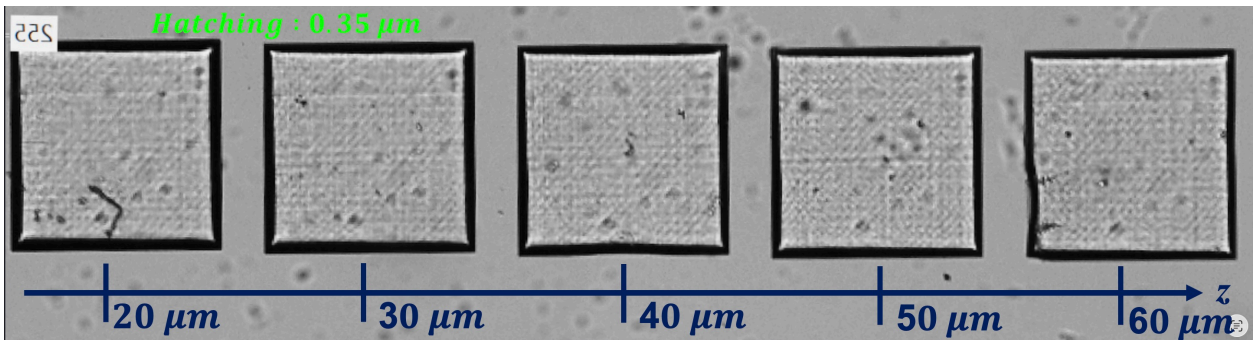

Figure 19: Optical microscope image of polymerized solid cuboidal blocks of varying vertical height and reduced hatching and slicing parameters to $\Delta H = \Delta Z = 0.35\ \mu m$. These structures were fabricated with the optimal laser power and scanning velocity parameters of $P = 0.15$ mW and $v = 1$ mm/s respectively

The results demonstrate that reducing the hatching and slicing values by half significantly improved the structural quality of the fabricated microstructures by increasing the voxel overlap, providing sufficient structural strength to the cuboidal blocks, and enhancing the degree of cross-linking of the polymerized regions, allowing them to withstand the development process without exhibiting cracking, deformation or internal damage. This is shown schematically in Fig. 20

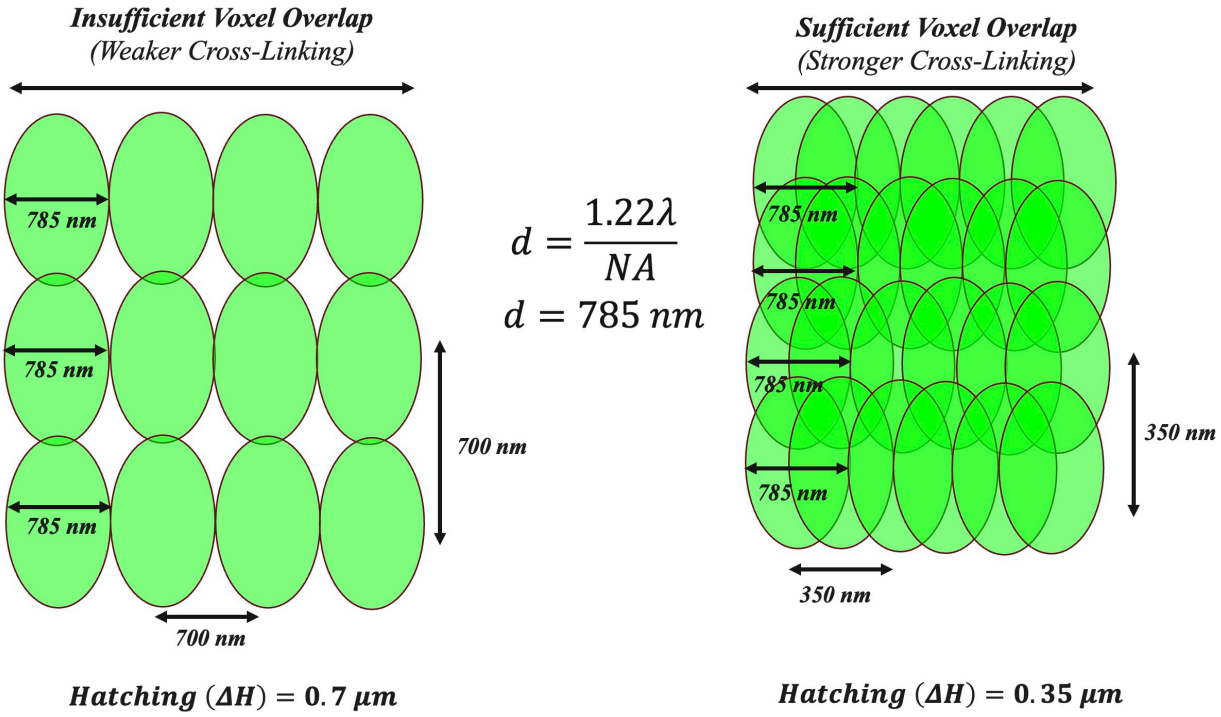

Figure 20: 2D Schematic diagrams showing a comparison between the voxel overlap observed with hatching parameter of $\Delta H = 0.7\,\mu m$ (a) and $\Delta H = 0.35\,\mu m$. The diagrams clearly indicate that higher hatching parameters, close to theoretical voxel size of $785\,nm$ leads to insufficient voxel overlap and thus weaker cross-linking, in contrast to much smaller hatching parameters of $300\,nm$ (b).

4.2 Rectangular Array of Cuboidal Blocks

Once the preliminary tests were completed, and the minimum laser power required for the production of mechanically stable cuboidal blocks had been identified, along with the appropriate hatching and slicing parameters necessary for sufficient voxel overlap, the fabrication substrate was switched from borosilicate glass to quartz glass. The primary reason for this transition was the thermal limitation of borosilicate glass [54]. Borosilicate glass exhibits a softening point at 800^oC, with an annealing point at 500^oC, whereas the minimum temperature required to achieve true ceramics during pyrolysis is 1000^oC. Consequently, borosilicate glass proved to be sufficient for preliminary tests, however it was unsuitable for the high temperature pyrolysis due to risk of substrate instability and deformation.

Quartz glass on the other hand possesses significantly improved thermal properties, exhibiting its softening point at 1600^oC with an annealing point at 1100^oC, making it substantially more suitable for high temperature thermal processing [55]. Moreover, both borosilicate glass and quartz glass exhibit refractive indices close to $n = 1.46$ at the operating laser wavelength of $\lambda = 515\,nm$, which closely matches the refractive index of the hybrid resin used. As a result, switching to quartz substrate did not involve the introduction of significant optical mismatches. Regardless, it was necessary to test the optimal laser parameters on quartz, by utilizing the data obtained from the preliminary tests on borosilicate glass.

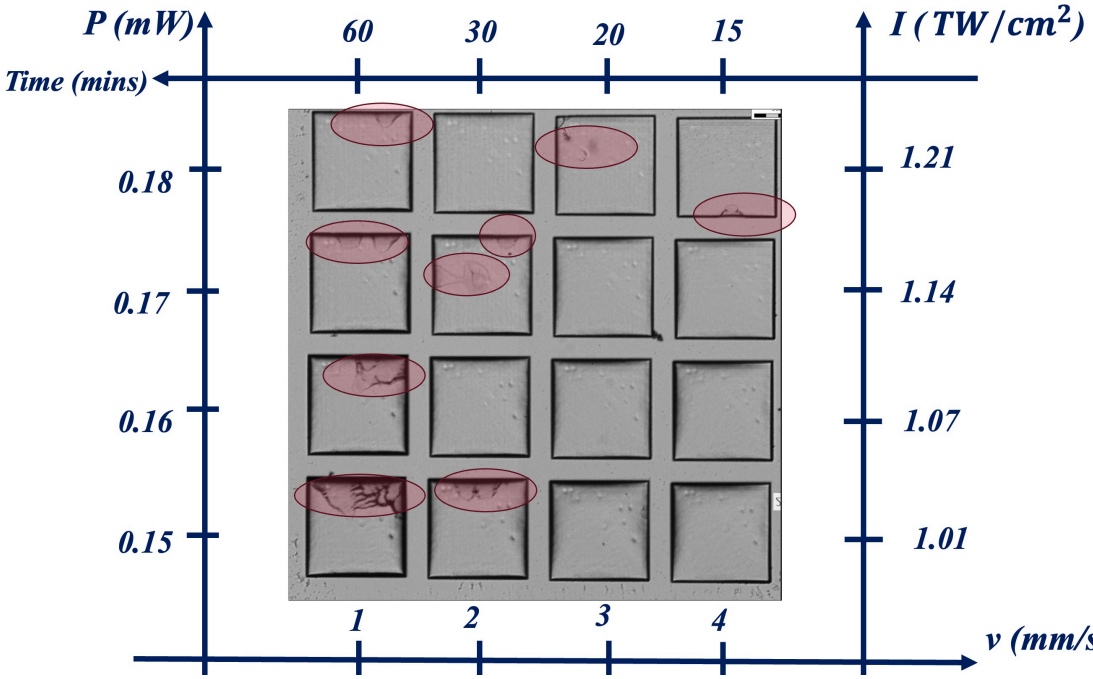

Figure 21: Optical microscope image of rectangular grid of solid cuboidal blocks, with dimensions 300x300x20 μm^3, fabricated by varying power along one axis of the grid from $P = 0.15 - 0.18$ mW with a step of $\Delta P = 0.01$ mW, and varying the scanning velocity along the other axis from $v = 1 - 4$ mm/s with a step of $\Delta v = 1$ mm/s. The highlighted red spots indicate the deformations developed in the structures post development

Fig. 21 shows the result of the fabrication of the rectangular grid of solid cuboidal blocks. The grid demonstrates the fabrication of the structures by simultaneously varying the laser power and laser scanning velocity along the two axes of the grid. It is evident that the parameters on quartz are not the same as the parameters on borosilicate glass, hence it was essential to perform the fabrication of such a rectangular grid. The blocks fabricated with the lowest power and lowest scanning velocity show the maximum damage and deformation (highlighted in red)($P = 0.15$ mW and $v = 1$ mm/s), indicating insufficient supply of dose and weak cross-linking throughout the structure. The highest quality structures are the one printed with the highest power and highest scanning velocity ($P = 0.18$ mW and $v = 4$ mm/s). However even these particular structures show minor cracks and solvent penetration (highlighted in red), leading to internal structural loss. Hence another similar test was conducted, by fabricating the structures with even higher powers. The results are shown in Fig. 22

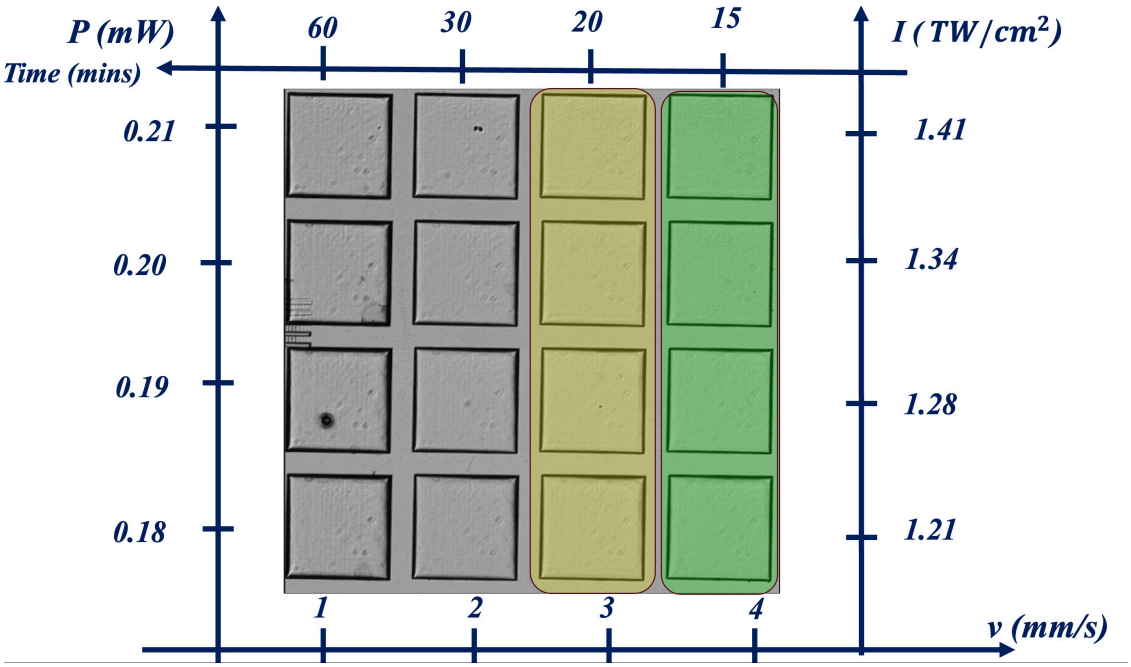

Figure 22: Optical microscope image of rectangular grid of solid cuboidal blocks, with dimensions 300x300x20 μm^3, fabricated by varying power along one axis of the grid from $P = 0.18 - 0.21$ mW with a step of $\Delta P = 0.01\, mW$, and varying the scanning velocity along the other axis from $v = 1 - 4$ mm/s with a step of $\Delta v = 1$ mm/s. The highlighted green region shows the structures suitable for thermal treatment, while the highlighted yellow region shows the structures which were not selected for pyrolysis due to longer fabrication time

Fig. 22,demonstrates that increasing the laser power dose has improved the quality of the fabricated structures, resulting in reduced cracking and deformations along with enhanced structural stability. The cuboidal blocks fabricated with high scanning velocity of $v = 3\, mm/s$ and $v = 4\, mm/s$ were suitable for the pyrolysis process (highlighted in yellow and green), however, the structures fabricated with the higher laser scanning speed were chosen, to reduce the fabrication time, and to ensure the blocks have high surface smoothness and strength to withstand both the development and the high temperature treatment during the pyrolysis process

4.3 Thermal Treatment- Pyrolysis

4.3.1 Obtaining the Opaque Microstructures

Following the optimization of the fabrication process, the next stage involved the high-temperature thermal treatment of the structures through pyrolysis. This step is critical for transforming the polymerized hybrid organic-inorganic structures into completely inorganic and opaque ceramic microstructures. The first pyrolysis test was performed at 1000^oC, with a temperature ramp of $5^oC/min$, in an inert nitrogen atmosphere, and the results of the pyrolysis are shown in Fig. 23. The image suggests that the pyrolyzed structures are indeed strongly absorbent of white light. However, all of the fabricated structures exhibited severe cracking, and two of the cuboidal blocks of vertical height $z = 5\,\mu m$ and $z = 10\,\mu m$ detached from the substrate. A plausible cause of the destruction of the blocks was attributed to the temperature ramp of $5^oC/min$. This heating rate may have been too high for the selected geometry of the polymerized structures, causing rapid material shrinkage in the fabricated structures during pyrolysis. If the structures did not undergo sufficient polymerization during fabrication, the internal stress developed during the mass loss may have exceeded the mechanical stability of the structures under the rapid thermal gradient. This likely lead to intense cracking and eventual detachment of the structures from the quartz due to shrinkage of the polymerized blocks, while the quartz maintains it original geometry.

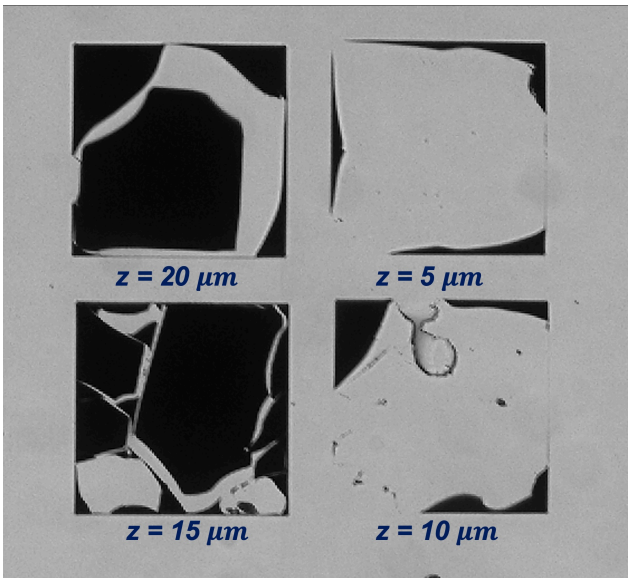

Figure 23: Optical microscope image of the polymerized microstructures of lateral dimensions $300 \times 300\,\mu m^2$ after thermal treatment. These structures were fabricated at laser power $P = 0.19\,mW$, laser scanning velocity $v = 4\,mm/s$, with similar hatching and slicing values of $\Delta H = \Delta Z = 0.35\,\mu m$. They underwent pyrolysis at 1000^oC in an inert nitrogen atmosphere with a temperature ramp of $5^oC/min$

Hence in order to reduce the internal stress developed within the structures and their subsequent cracking and detachment, the structures were fabricated again, but with a slightly higher laser power of $P = 0.21\,mW$, to ensure that the dose provided to the structures was

sufficient to withstand the stresses of heat treatment. The remaining fabrication parameters were retained, with the laser scanning velocity of $v = 4\,mm/s$, and similar hatching and slicing values of $\Delta H = \Delta Z = 0.35\,\mu m$. Some of the polymerized structures prepared for pyrolysis are shown in Fig. 24

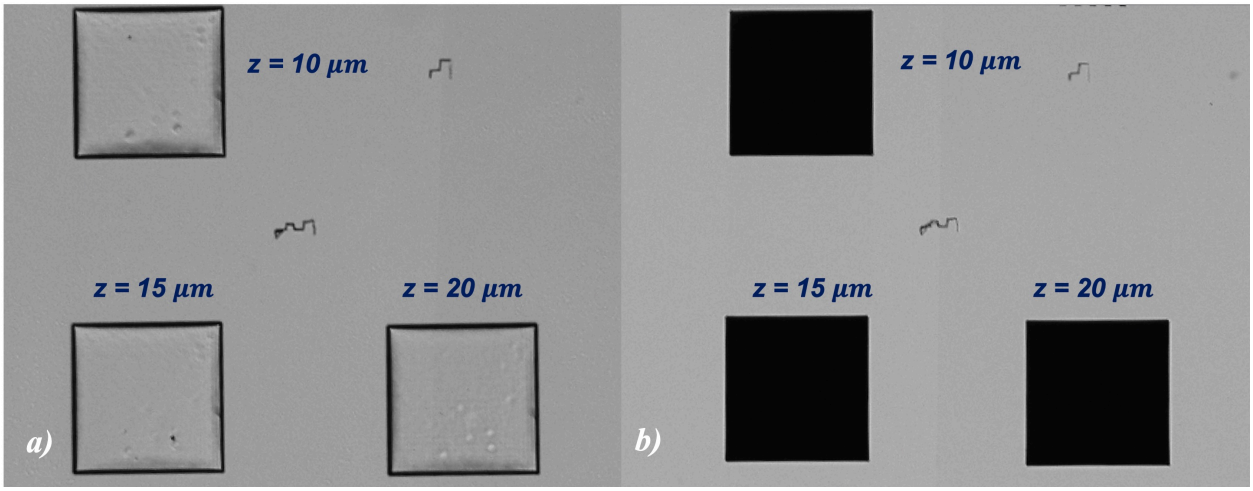

Figure 24: a) Optical microscope image of the polymerized cuboidal blocks of vertical height varying from $z = 10 - 20\,\mu m$, with lateral dimensions $300 \times 300\,\mu m^2$ that survived the development process. (Cuboid of height $z = 5\,\mu m$ is not visible in this image, but it was also fabricated and it survived the heat treatment) b) Optical microscope image of the same polymerized cuboids post thermal treatment, pyrolyzed at 1000^oC at a rate of $1^oC/min$ in an inert nitrogen atmosphere

From Fig. 24, it is evident that reducing the temperature ramp from $5^oC/min$ to $1^oC/min$ was essential to reduce the internal stresses developed during pyrolysis, and also to ensure gradual evaporation of the organics, while simultaneously promoting uniform volumetric shrinkage throughout the block. Since the polymerized structures show rapid reduction in mass during the decomposition phase between $300^oC - 600^oC$, [37] a slower temperature ramp played a significant role in maintaining the structure morphology and reduce the formation of cracking. The increased laser power of $P = 0.21mW$ also played a role in the prevention of cracking and deformations in the structure, by ensuring sufficient polymerization of the cuboidal blocks. The heating temperature of 1000^oC was selected by keeping in mind both, the temperature limitations of the quartz substrate, along with the results reported in previously published literature on the hybrid resin [37]. These studies demonstrated that pyrolysis at 1000^oC leads to the complete elimination of the organic components, along with the formation of silicon oxycarbide composite networks, resulting in optically opaque or 'black' microstructures. SEM images of the structures obtained post pyrolysis are shown in Fig. 25

4.3.2 Surface Roughness

The structures were analyzed using the optical profilometer for surface roughness before and after the heat treatment to evaluate the influence of the heating process on the characteristics of the surface morphology. The average surface roughness of the structures (R_a) before and after pyrolysis are presented in the Tab. 1

Table 1: Average surface roughness values before and after pyrolysis for each cuboidal microstructure.

Structure height (μm)	R_a before pyrolysis (μm)	R_a after pyrolysis (μm)	Improvement
5	0.219 ± 0.074	0.213 ± 0.030	2.7%
10	0.314 ± 0.165	0.300 ± 0.010	4.5%
15	0.277 ± 0.029	0.236 ± 0.020	14.8%
20	0.247 ± 0.071	0.186 ± 0.030	24.7%

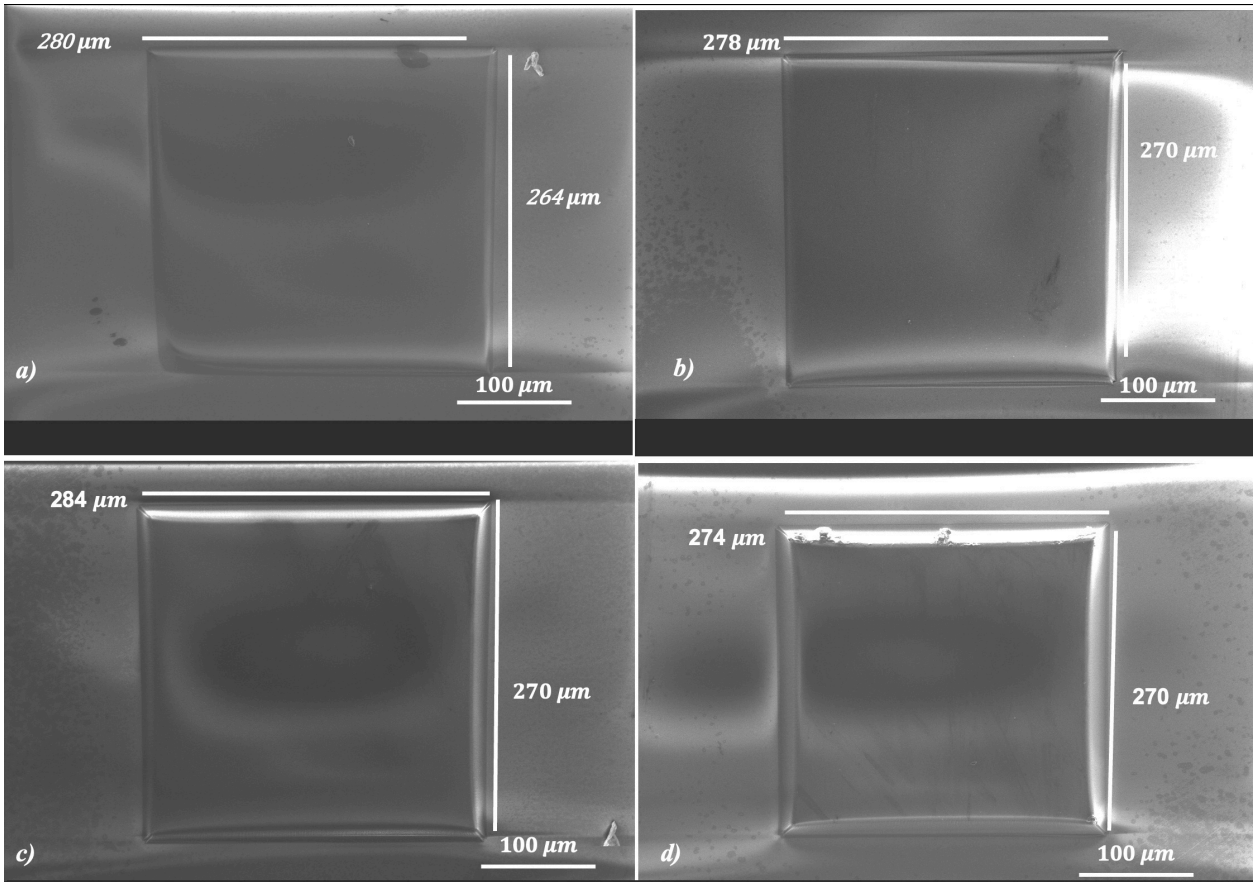

Figure 25: SEM images of the fabricated solid cuboidal blocks of vertical heights $z = 5\,\mu m$ (a), $z = 10\,\mu m$ (b), $z = 15\,\mu m$ (c) and $z = 20\,\mu m$ (d). Images taken post pyrolysis

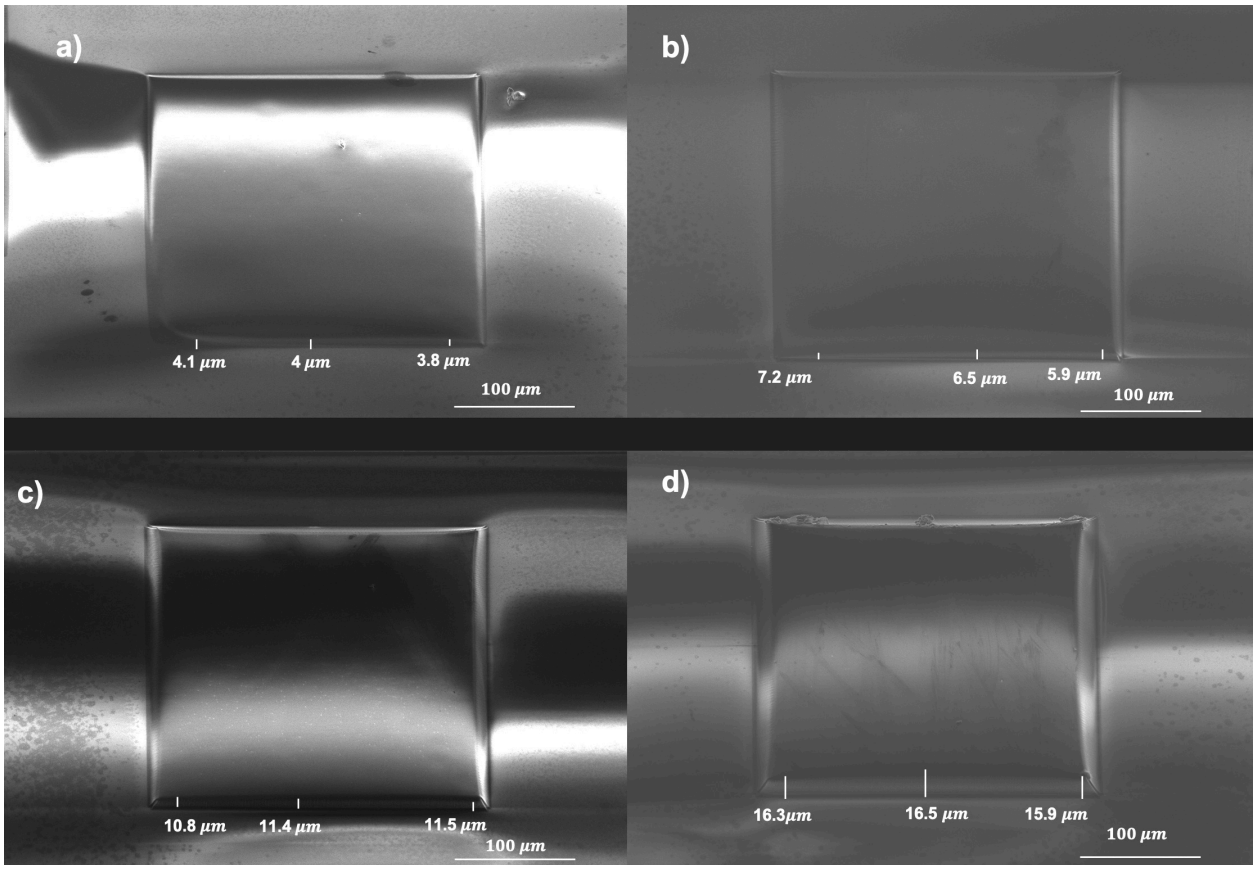

Figure 26: SEM images of the fabricated solid cuboidal blocks, tilted at 30^o angle for vertical heights $z = 5\,\mu m$ (a), $z = 10\,\mu m$ (b), $z = 15\,\mu m$ (c) and $z = 20\,\mu m$ (d)

The trend observed in Tab. 1 suggests that the heat treatment did not degrade the surface quality of the fabricated structures. Instead, the decrease in surface roughness observed may indicate an increase in the densification of the polymer networks and surface smoothing during the polymer to ceramic conversion. The reduction of R_a can be attributed to the removal of the organic content of the structure along with the subsequent consolidation of the inorganic networks during pyrolysis. The shrinkage and consolidation of the inorganic networks can reduce the surface irregularities and lead to a more compact ceramic structure. However, it is important not to overestimate the effect of the heat treatment on the surface roughness, since the uncertainty ranges of some measurements overlap. Hence rather than indicating a drastic change in the surface roughness of the structure, the data more reliably suggests pyrolysis assisted in preserving the overall surface morphology of the structures, while producing a slight smoothing effect. This is an important observation since high-temperature thermal treatment frequently produces cracks and deformations, or degradation, while here we observe the surface quality to have improved post pyrolysis. The SEM images of the pyrolyzed cuboidal blocks are shown in Fig. 25, and the images clearly indicate the absence of any structural deformations such as severe cracking or solvent penetration.

4.3.3 Shrinkage

Due to the high temperatures achieved during the pyrolysis process, the organics are completely eliminated from the microstructures, causing significant mass loss in the fabricated structures. This loss in mass is realized in the structures as a volumetric shrinkage, which is a commonly observed outcome of thermal treatment of structures polymerized using hybrid organic-inorganic resins. The cuboidal blocks fabricated in this study were also analyzed for shrinkage using the optical profilometer and the SEM, where the reduced vertical heights were observed and the shrinkage ratios were calculated which are displayed in Tab. 2

Table 2: Reduction in vertical height after pyrolysis and their corresponding shrinkage ratios.

Vertical height of structure (μm)	Reduced height post pyrolysis (μm)	Shrinkage ratio
5	3.96 ± 0.6	0.2
10	6.5 ± 1.06	0.34
15	11.23 ± 1.7	0.25
20	16.08 ± 1.1	0.2

The shrinkage measurements demonstrated in Tab. 2 indicate that all fabricated structures underwent significant mass loss and consequent reduction along the vertical axis of the cuboidal block, with the shrinkage ranging between 20% – 34%. This is characteristic behavior for the conversion of hybrid organic-inorganic polymerized structures to ceramic via pyrolysis, where the decomposition of the organic content and the subsequent densification of the inorganic networks leads to the volumetric reduction of the microstructures. Despite the relatively large shrinkage ratios observed for all the cuboidal blocks, the structures retained their structural morphology without any cracks, indicating that the selected fabrication and pyrolysis parameters were sufficient for efficient development and conversion of opaque ceramics microstructures. However, no clear relationship between the initial structure height and the resulting shrinkage ratio was observed. The variation in the vertical shrinkage ratios may suggest that the reduction in size is not solely governed by the structure height, but also by substrate constraint, polymerization density, volatile gas release and internal stress distribution. The strong adhesion of the structures to the quartz substrate provided different constraints to the different vertical shrinkage of the structures, causing nonuniform shrinkage across the structures. Therefore, the differences in the shrinkage ratio should be interpreted as a result of spatially nonuniform densification rather than a simple height dependent trend. But it is important to note that even the lateral dimensions undergo shrinkage, and the observed shrinkage along the lateral dimensions of the fabricated cuboidal blocks is shown in Tab. 3 for shrinkage along the X dimension and Tab. 4 for shrinkage along the Y dimension.

Table 3: Reduction in the lateral X direction of the fabricated structures after pyrolysis and their corresponding shrinkage ratios.

Vertical height of structure (μm)	Initial lateral dimension along X-Axis (μm)	Reduced lateral dimension post pyrolysis (μm)	Shrinkage ratio
5	300	277.2 ± 7.01	0.08
10	300	273.5 ± 6.4	0.09
15	300	279.5 ± 6.4	0.07
20	300	273 ± 1.4	0.09

Table 4: Reduction in the lateral Y direction of the fabricated structures after pyrolysis and their corresponding shrinkage ratios.

Vertical height of structure (μm)	Initial lateral dimension along Y-Axis (μm)	Reduced lateral dimension post pyrolysis (μm)	Shrinkage ratio
5	300	265.3 ± 2.8	0.12
10	300	271.4 ± 1.4	0.1
15	300	268.5 ± 2.1	0.1
20	300	251.5 ± 2.1	0.16

The data in Tab. 3 and Tab. 4 indicate the shrinkage exhibited by the fabricated structures is anisotropic. Such behavior is commonly observed in structures that have strong attachment or adhesion to the substrate. This adhesion restricts the lateral contraction, while allowing larger contraction along the vertical dimensions of the structure. In addition to the anisotropic shrinkage between the vertical and lateral dimensions, the data also reveal lateral asymmetry within the structures. Along the X direction, the opposite sides of the blocks do not shrink equally for the $5\,\mu m$, $10\,\mu m$ and $15\,\mu m$ blocks. This is explained by the relatively large uncertainty values observed in Tab. 3. In these structures, the difference in the reduced lengths of the opposite sides along the X axis was observed to be as large as $10\,\mu m$, indicating that the shrinkage was not spatially uniform along the same lateral direction. Hence the uncertainty values do not simply express the instrument measurement error, but instead reflect real asymmetry produced due to the shrinkage. In contrast, the shrinkage along Y axis appears to be considerably more symmetric, which is indicated by the smaller uncertainty values in Tab. 4, where the opposite sides of the block along the Y axis exhibit more comparable reduction in dimensions. Also, the shrinkage ratios along the Y axis are generally larger than those observed for the X direction, suggesting that the lateral contraction is also directionally dependent. Hence the structures not only exhibit anisotropic shrinkage between the different planes, but also show asymmetric shrinkage within the same plane.

However, an interesting observation shows that this asymmetric shrinkage becomes less pronounced for the $20\,\mu m$ structure. In contrast to the shorter structures, the $20\,\mu m$ block exhibits a much smaller uncertainty along the X direction, indicating the two opposite sides along the X direction experienced more uniform shrinking, suggesting that the shrinkage behavior becomes more uniform for taller structures. A plausible explanation for such behavior could be directly related to the development and distribution of internal stresses during pyrolysis. For the shorter structures, the strong attachment and adhesion to the quartz substrate may dominate the shrinkage behavior, strongly restricting the contraction differently along different points of the structure, leading to asymmetric stress. Small variations such as fluctuations in voxel overlap, laser exposure does, or the cross-linking density might be the cause for such asymmetries experienced during the pyrolysis process. However, as the structures grow taller, the influence of the substrate induced constraints may become less dominant, relative to the overall large volume of the structure, allowing a more effective redistribution of the internal stress, resulting in a more uniform lateral shrinkage. Further experimentation is necessary to confirm whether the observed behavior is maintained for structures taller than $20\,\mu m$, which can be checked by fabricating taller solid cuboidal blocks with the same laser parameters and treating them thermally with the same parameters selected for pyrolysis. If the taller blocks also exhibit the similar behavior of uniform lateral shrinkage, then one can confidently say that internal stress distribution become more dominant than the substrate induced constraints relative to the overall volume of the block.

4.4 Optical Transmission

Following the pyrolysis process, the optical transmission measurements were performed at two wavelengths, $\lambda_1 = 633\,nm$ and $\lambda_2 = 510\,nm$. As the laser beam of the selected wavelength passes through the fabricated structures, the transmitted beam signal was split between a camera, which allowed real-time visualization of the beam, and a photodiode, which measured the transmission signal through the opaque ceramics. Another photodiode placed before the structures acted as a reference value for the transmitted signal as shown in Fig. 13. The two signals formed the two input channels of the oscilloscope, where the signal transmitted through the fabricated structures was normalized by the reference beam signal in order to obtain the true transmission values for the opaque ceramic microstructures. Since the laser beam was also propagated through the quartz substrate during the measurements, the transmission signal obtained from the structures was first referenced against the transmission through the quartz substrate alone. This reference measurement allowed the absorption caused specifically by the opaque structures to be evaluated independently of the substrate contribution. The transmitted laser beam through the quartz substrate is shown in Fig. 27

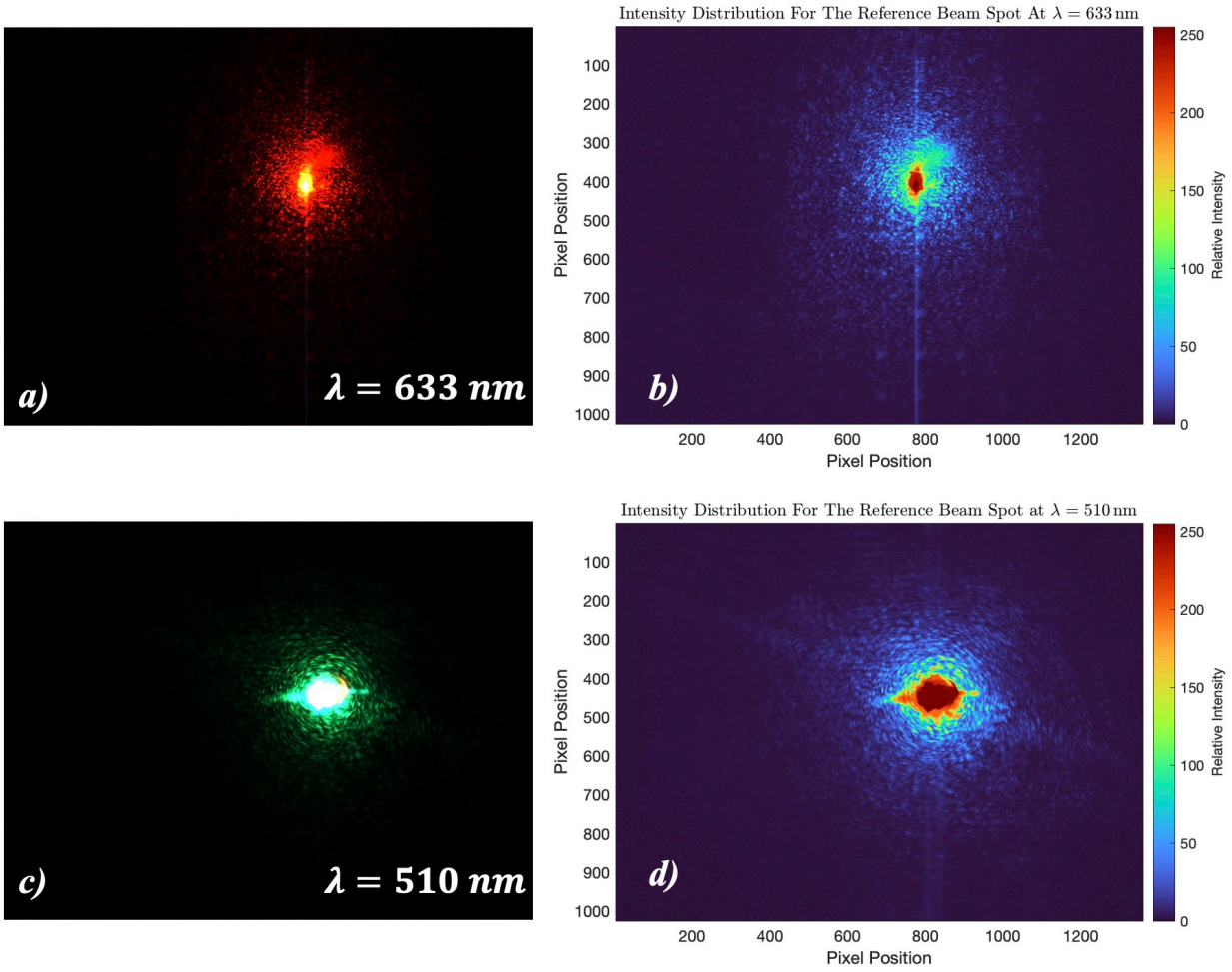

Figure 27: Camera images of the reference beam spot passing through quartz substrate (a,c), and heat map images of the reference beam spot generated using pixels from the original camera image (b,d)

Table 5: Evaluation of the transmitted signal for different wavelengths, normalized with respect to the reference beam signal, for propagation through air and quartz substrate.

Wavelength (nm)	Normalized signal passing through air (mU)	Normalized signal passing through quartz (mU)	Transmission (%)
633 nm	195	180	92%
510 nm	410	365	89%

The transmission data presented in Tab. 5 indicates that the quartz substrate exhibits high optical transparency at both the selected wavelengths. The relatively high transmission values confirm that quartz introduces minimal attenuation of the incident beam within the visible spectral range. However, a slight reduction in the transmission signal is observed for the shorted wavelength of $\lambda_2 = 510\,nm$ compared to $\lambda_1 = 633\,nm$. This behavior is physically expected and can explained by the wavelength-dependent optical losses through the system. Since shorter wavelengths are more strongly affected by scattering processes (Rayleigh Scattering), green light experiences slightly larger losses compared to red light. Furthermore, the refractive index of quartz also plays a role, as it exhibits wavelength dependence due to material dispersion, resulting in higher Fresnel reflection losses at shorter wavelengths. Nevertheless, the transmission values remain relatively high for both selected wavelengths, indicating that the quartz substrate has small or negligible contribution to the overall signal. Hence any reduction in the transmission signal observed after the introduction of the ceramic microstructures is relatively independent of the influence from the substrate, and can be attributed to the absorption and scattering induced by the fabricated structures.

4.4.1 Red Light ($\lambda_1 = 633\,nm$)

For each wavelength, the signal for the normalized beam spot passing through quartz was calculated, denoted as R_Q, along with the noise signal, denoted as N, which indicated the normalized signal calculated by the oscilloscope even when the measuring diode was blocked (D2 in Fig. 13). Thus the transmission measurements for $\lambda_1 = 633\,nm$ for the cuboidal blocks of varying heights are shown in Tab. 6

The transmission data presented in Tab. 6 together with Fig. 28 demonstrates that the pyrolyzed ceramic microstructures strongly absorb the light propagating through them at $\lambda = 633\,nm$. The transmission values were calculated by taking into account the normalized reference signal through quartz (R_Q), and the normalized background noise signal detected by the oscilloscope when no light was incident on the diode (N). The reference signal through quartz varied slightly at different points on the substrate, but the system showcased a constant background noise at $N = 0.4108\,mU$. As seen from the data, the cuboidal blocks of vertical heights $z = 10\,\mu m$, $z = 15\,\mu m$ and $z = 20\,\mu m$ produced transmission signals that were indistinguishable from the background noise level, thus denoting the transmission

Table 6: Optical transmission measurements at $\lambda_1 = 633\,nm$ of the pyrolyzed ceramic microstructures for different structure heights, normalized with respect to the quartz reference signal and background noise.

Vertical height of the structure (μm)	Quartz Signal, R_Q (mU)	Noise signal, N (mU)	Signal through structure, R_S (mU)	$T(\%) = \left(\frac{R_S - N}{R_Q - N}\right) \times 100$
5	167.5	0.4108	1.973	0.93%
10	175.4	0.4108	0.4108	0%
15	180.3	0.4108	0.4108	0%
20	180.5	0.4108	0.4108	0%

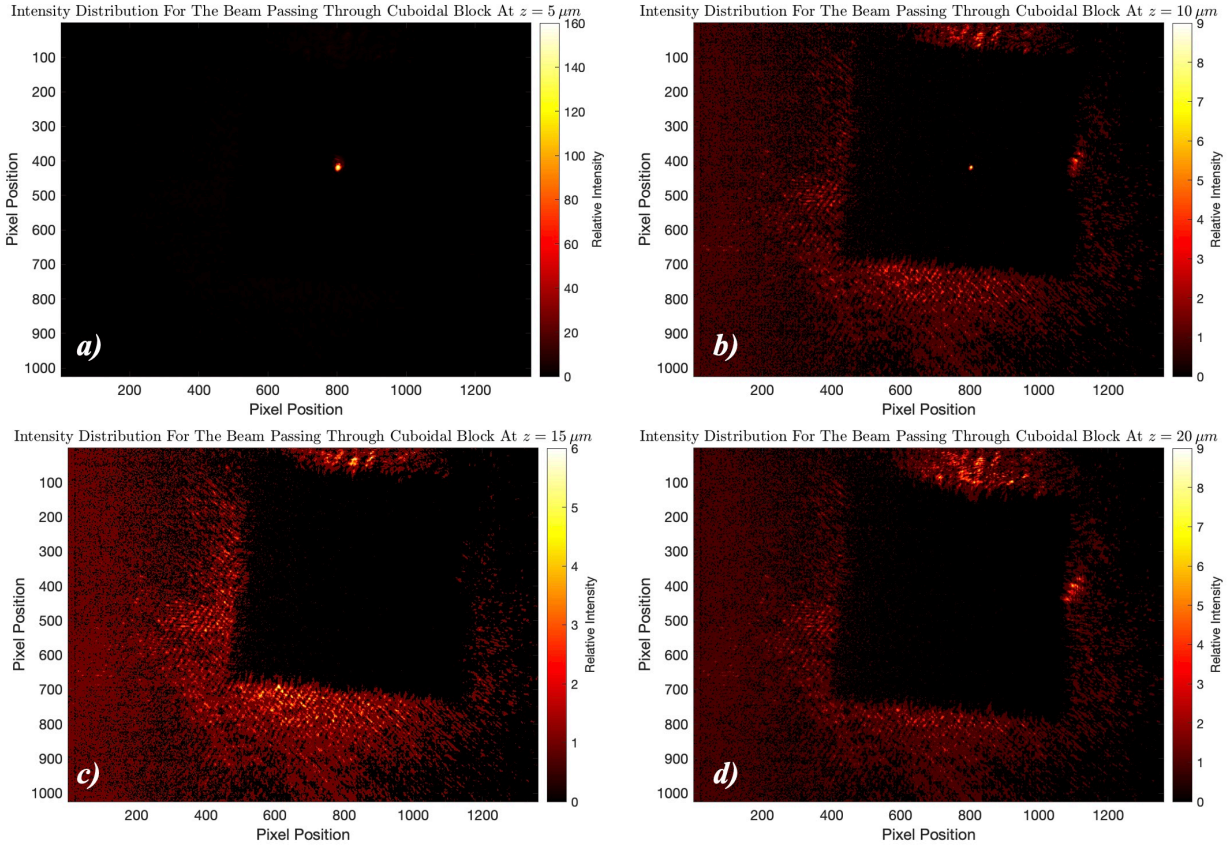

Figure 28: Heat map intensity distribution of the laser beam passing through the pyrolyzed microstructure of vertical height $z = 5\,\mu m$ (a), $z = 10\,\mu m$ (b), $z = 15\,\mu m$ (c), $z = 20\,\mu m$ (d)

as 0%. This data is also confirmed qualitatively from the intensity distribution heat map of the camera image in the Fig. 28c and Fig. 28d. However, the structure in Fig. 28b still exhibits a weak residual transmitted signal, despite the transmission signal calculated by the oscilloscope indicating 0%. This implies that the transmitted signal was below the detection limit of the photodiode-oscilloscope measurement setup and could not be resolved reliably above the noise detected. By taking the noise signal $N = 0.4108\,mU$ and the reference signal

as $R_Q = 180\,mU$, we see that the transmission limit is give by:

$$T_{lim}^{\%} = \frac{N}{R_Q - N} \times 100 = \frac{0.4108}{180 - 0.4108} \times 100 = 0.22\% \tag{13}$$

Thus Eqn. 13 shows that the measurement limit for the photodiode-oscilloscope measurement setup for $\lambda = 633\,nm$ is 0.22%. Thus any transmission signal below this threshold, ($T < T_{lim}$) cannot be detected or measured reliably by the measurement setup, thus determining the sensitivity limit and precision of the conducted measurements. For the $5\,\mu m$ structure however, both the qualitative as well as quantitative data agree that a measurable signal was able to be transmitted through the structure to be detected by the photodiode and be analyzed by the oscilloscope. Nevertheless, since the measured transmission signal lies close to the detection limit of the oscilloscope-based setup, the calculated transmission value may still be affected by reduced accuracy relative to the true transmissted intensity.

4.4.2 Green Light ($\lambda_2 = 510\,nm$)

The same set of measurements were performed for $\lambda_2 = 510\,nm$ for the cuboidal blocks of varying heights, and the results are shown in Tab

Table 7: Optical transmission measurements at $\lambda_2 = 510\,nm$ of the pyrolyzed ceramic microstructures for different structure heights, normalized with respect to the quartz reference signal and background noise.

Vertical height of the structure (μm)	Signal through quartz, R_Q (mU)	Noise signal, N (mU)	Signal through structure, R_S (mU)	$T(\%) = \left(\frac{R_S - N}{R_Q - N}\right) \times 100$
5	359.4	8.5	8.5	0%
10	360.5	8.5	8.5	0%
15	365.7	8.5	8.5	0%
20	365.2	8.5	8.5	0%

The transmission data presented in Tab. 7 together with Fig. 29 demonstrates similar behavior as observed for red light. These values were calculated using the same procedure and calibration as for red light. The quantitative data indicates that for $\lambda_2 = 510\,nm$, all the structures produced transmission signals that were indistinguishable from the noise signal obtained when the diode was blocked, thus indicating a transmission of 0%. However, in Fig. 29a, we observe a small residual signal that penetrates through the structure and is detected by the camera, and hence highlighted in the intensity distribution map as well. However, this signal was also below the detection limit of the setup and was too weak to be resolved by the oscilloscope. By considering the noise signal $N = 8.5\,mU$ nd the reference signal as $R_Q = 365.2\,mU$, we see that the transmission limit is give by:

$$T_{lim}^{\%} = \frac{N}{R_Q - N} \times 100 = \frac{8.5}{365.2 - 8.5} \times 100 = 2.38\% \tag{14}$$

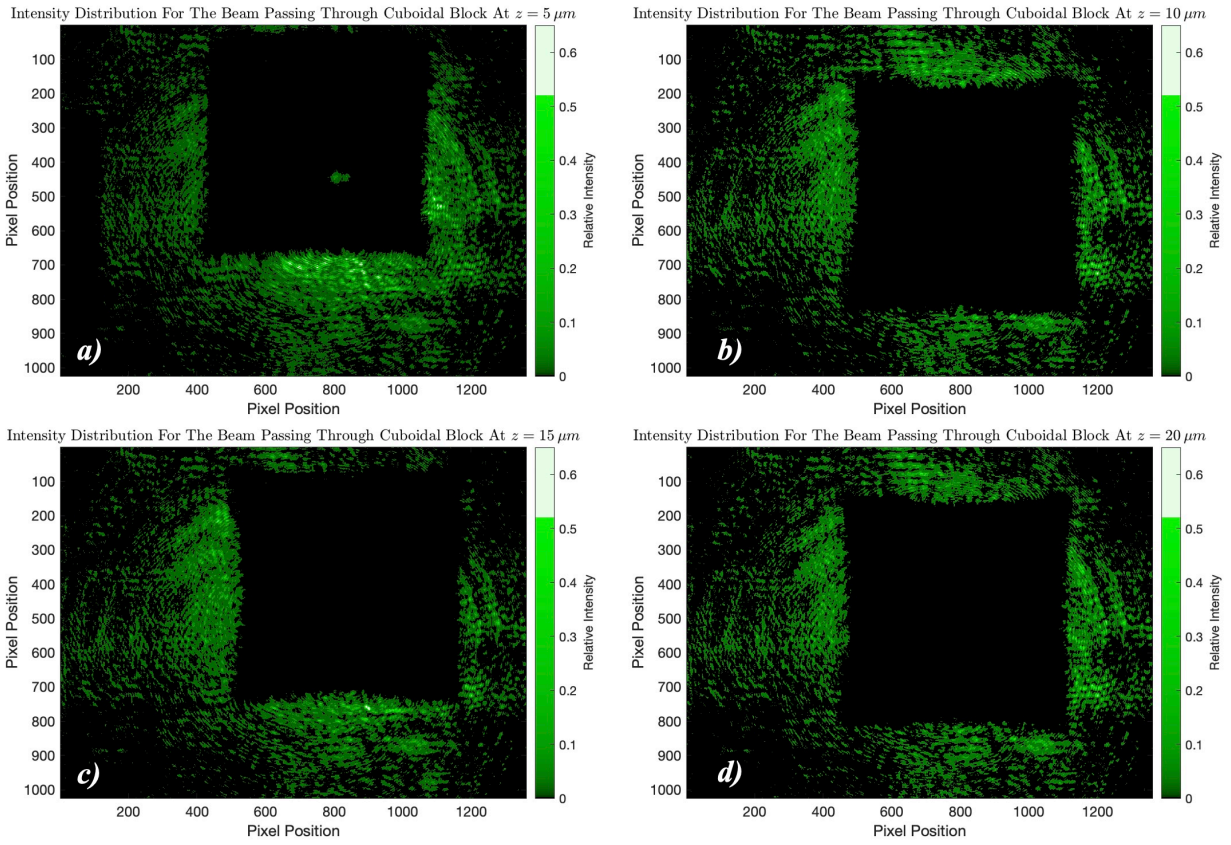

Figure 29: Heat map intensity distribution of the laser beam passing through the pyrolyzed microstructure of vertical height $z = 5\,\mu m$ (a), $z = 10\,\mu m$ (b), $z = 15\,\mu m$ (c), $z = 20\,\mu m$ (d)

Thus Eqn. 14 shows that the measurement limit for the photodiode-oscilloscope measurement setup for $\lambda = 510\,nm$ is 2.38%. It is important to note that this threshold limit for reliable measurements is higher for green light than for red light, which may be attributed to the higher noise signal recorded during the measurements. Thus any signal below this threshold cannot be analyzed by the oscilloscope, thus limiting the precision and accuracy of the transmission signals. Although the qualitative data acquired via the transmission measurements were limited by the precision and accuracy of the measuring equipment, the quantitative data obtained from the camera images and processed into intensity distribution provides sufficient evidence which shows the strong absorbing nature of the structures post pyrolysis. Future steps involves utilizing the strong absorption properties of the structures to test their applications in microoptics for preparing amplitude masks, beam blockers, absorbers and stray light .

5 Comparison with Published Work

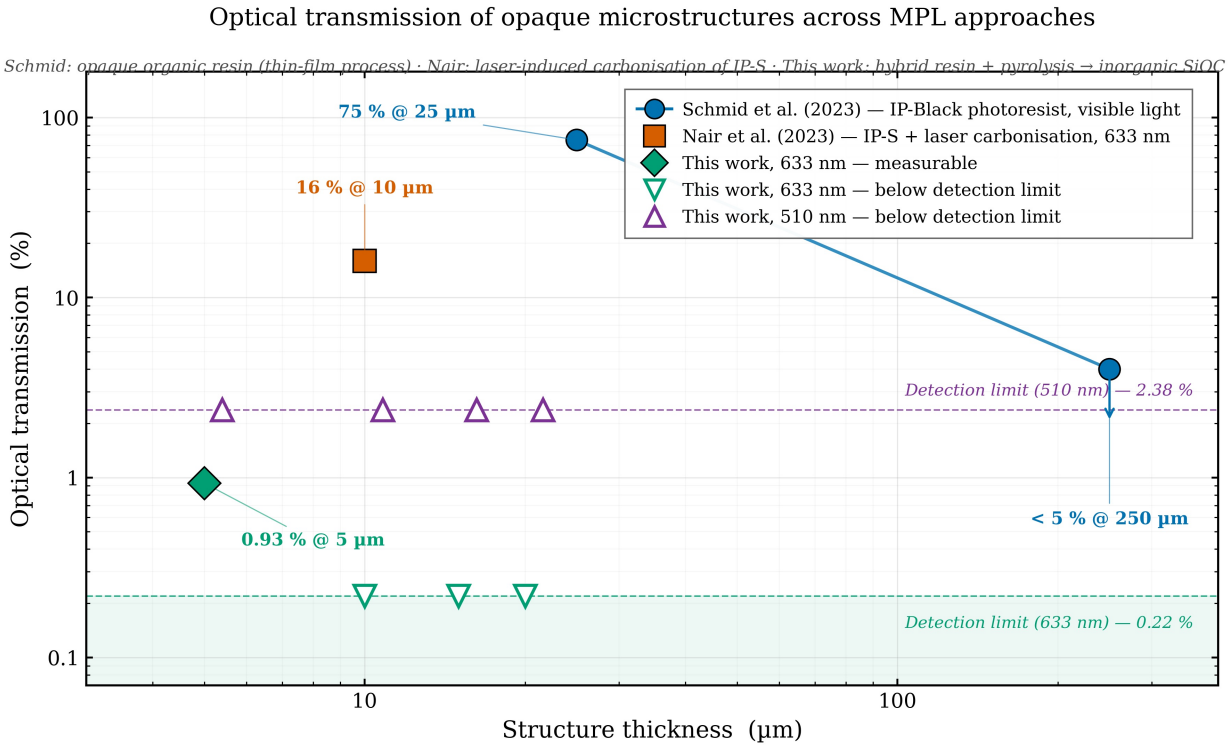

Figure 30: Graphical representation providing a comparison of the optical transmission achieved in the visible spectrum as a function of the thickness of the microstructures, fabricated by Schmid et al. [48], Nair et al. [17], and the present study

The two major studies investigating opaque microstructures employ fundamentally different approaches and consequently achieve different levels of optical performance and structural quality. Schimd et al. [48] utilized the commercially available organic photoresist IP-Black directly during fabrication, which is a resin specifically designed for light suppression. In contrast, Nair et al. [17] employed a standard transparent IP-S photoresist and generated opaque regions through laser-induced carbonization of the polymer during the fabrication process. Their main approach was to achieve both transparent and opaque microstructures within the same fabrication process employing multiphoton lithography.

Schmid et al. [48] demonstrated strong attenuation of visible light, achieving transmission values upto 75% for structures with thickness of $25\,\mu m$, with the transmission dropping below 5% for structures that are $250\,\mu m$ thick, indicating that complete optical absorption was not perfectly achieved throughout the structures. In comparison to that, the structures fabricated in this study using the hybrid organic and inorganic resin demonstrate significantly stronger optical attenuation, achieving complete optical absorption with transmission values of 0%, with considerably smaller thickness of $10\,\mu m$ for the fabricated structures, suggesting that the pyrolysis based approach developed in the present work produces significantly stronger light suppression, even for thinner microstructures.

On the other hand, Nair et al. [17] were successfully able to fabricate opaque structures

through laser overexposure, generating black carbonized structures, and achieving transmission values up to 18% for structures of $10\,\mu m$ thickness. However, their study also mentioned the presence of significant structural instabilities associated with laser decomposition, including bubble formation, local damage, rough interfaces, and geometric deformation of the fabricated structures. In contrast, structures fabricated in the present study did not exhibit any observable surface deformation or structural decomposition following the pyrolysis process. SEM analysis instead revealed comparatively smoother structures which retained their original structural shape, indicating that the pyrolysis-based approach of obtaining opaque microstructures may provide improved structural stability and also simultaneously achieve stronger optical attenuation. Furthermore, the fabrication process in this study takes place in a much more controlled manner as compared to randomized overexposure, thus providing higher quality structures.

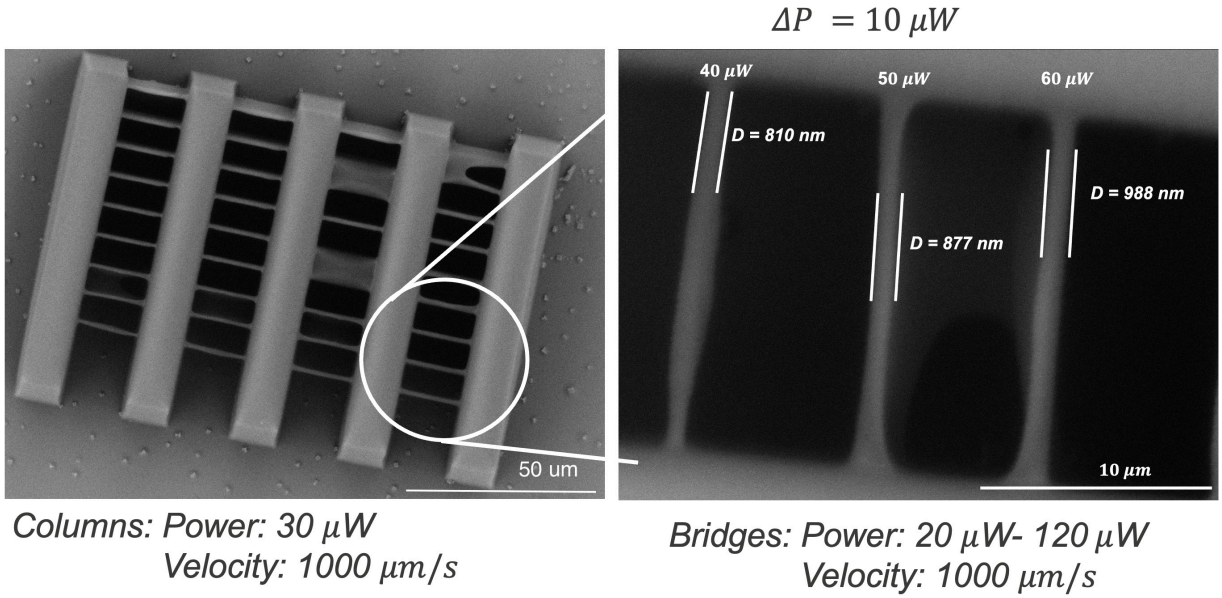

Figure 31: Fabricated resolution bridges indicating the smallest feature sizes which were fabricated are close to the theoretical value of the voxel, indicating agreement between the theory and experiment, and also the capability to achieve higher resolution by using higher NA objectives

Fig. 31 indicates that voxel size obtained for laser power $P = 0.04\,mW$, and scanning velocity $v = 1\,mm/s$, produce a voxel of lateral size closely comparable to the theoretically calculated size. Although the final cuboidal structures that were fabricated and treated thermally were not fabricated using the exact same parameters as the resolution bridges, the scanning parameters were scaled approximately proportionally in both laser power and scanning velocity. For the fabrication of the cuboidal blocks, the laser powers and scanning velocities used were increased approximately by a factor of 4 ($P = 0.21\,mW, v = 4\,mm/s$). While the linear exposure dose remained the same, the voxel size may not have been the same, since two-photon polymerization is a nonlinear process. Regardless, the resulting increase in the voxel size is expected to be small, which may explain why the similar hatching and slicing parameters could still enable successful fabrication of the cuboidal blocks.

Thus the structures fabricated in this study exhibit the strongest absorption in the tested wavelengths ($\lambda_1 = 633\,nm$ and $\lambda_2 = 510\,nm$) out of any of the structures reported in literature (to the best of my knowledge). These structures showcase higher opacity at significantly shorter dimensions, improved surface quality, and are also expected to demonstrate higher damage threshold due to the inorganic content as demonstrated by previous studies on similar materials [56].

Future work involves investigating the transmission values of the pyrolyzed structures using infrared and UV wavelengths, to test whether the structures are able to absorb wavelengths outside the visible spectrum as well. More testing will be conducted on the inorganic nature of the pyrolyzed structures, to quantify their damage thresholds and durability in extreme environments. Along with that, the resin will also be tested for the fabrication of the smallest feature sizes achievable, by employing higher NA objectives to fabricate smaller features and increase the resolution. Finally, the structures will be tested for future applications in microoptics, by the additive manufacturing of UV masks, beam blockers and stray light suppressors.

6 Conclusions

1. Optimal laser parameters identified for the fabrication of **solid microstructures** with lateral dimensions of $\mathbf{300 \times 300\,\mu m^2}$ indicate that **sufficient voxel overlap of** $\mathbf{350\,nm}$ close to the **theoretical voxel size of** $\mathbf{392\,nm}$ is necessary for the development of stable bulky microstructures.

2. Pyrolysis can lead to **improvement in surface quality by up to 24**%, provided the temperature ramp is $\mathbf{1^oC/min}$, and the structures are heated at $\mathbf{1000^oC}$ in an **inert nitrogen environment**.

3. The microstructures fabricated using multiphoton lithography exhibit strong absorption of visible light post pyrolysis , **absorbing up to 99.07**% **at** $\boldsymbol{\lambda = 633\,nm}$ and up to **100**% at $\boldsymbol{\lambda = 510\,nm}$, at $\boldsymbol{z = 5\,\mu m}$ with taller structures exhibiting **100**% absorption for both wavelengths, within the limitations of the measurement setup.

4. The optical opacity achieved in this study surpasses previously reported values in the literature while being realized at significantly smaller structure thicknesses while being achieved in ceramic materials.

References

[1] N. Guo and M. Leu, Additive manufacturing: Technology, applications and research needs, *Frontiers of Mechanical Engineering*, 2013, **8**, 215243.

[2] R. Vilar, ed., *Laser Surface Modification of Biomaterials: Techniques and Applications*. Woodhead Publishing / Elsevier, 2016.

[3] E.-S. Wu, J. H. Strickler, W. R. Harrell, and W. W. Webb, Two-photon lithography for microelectronic application, vol. 1674, 776 – 782, International Society for Optics and Photonics, SPIE, 1992.

[4] D. Gonzalez-Hernandez, S. Varapnickas, A. Bertoncini, C. Liberale, and M. Malinauskas, Micro-optics 3D printed via multi-photon laser lithography, *Advanced Optical Materials*, 2023, **11**, 2201701.

[5] O. Tsilipakos, G. Perrakis, M. Farsari, and M. Kafesaki, Polymeric optical metasurfaces by two-photon lithography: Practical designs for beam steering, in *2024 Eighteenth International Congress on Artificial Materials for Novel Wave Phenomena (Metamaterials)*, 1–3, 2024.

[6] G. van der Velden, D. Fan, and U. Staufer, Fabrication of a microfluidic device by using two-photon lithography on a positive photoresist, *Micro and Nano Engineering*, 2020, **7**, 100054.

[7] S. Yu, Q. Du, C. R. Mendonca, L. Ranno, T. Gu, and J. Hu, Two-photon lithography for integrated photonic packaging, *Light: Advanced Manufacturing*, 2023, **4**, 486–502.

[8] C. B. Arnold, Laser direct-write techniques for printing of complex materials, in *Proceedings of the SPIE*, vol. Vol. 6451, 64510A, 2007.

[9] S. O'Halloran, A. Pandit, A. Heise, and A. Kellett, Two-photon polymerization: Fundamentals, materials, and chemical modification strategies, *Advanced Science*, 2023, **10**, 2204072.

[10] A. Gaeta and R. Boyd, Nonlinear optics, basics | ultrafast and intense-field nonlinear optics, 258–262.

[11] A. Jaiswal, C. K. Rastogi, S. Rani, G. P. Singh, S. Saxena, and S. Shukla, Two decades of two-photon lithography: Materials science perspective for additive manufacturing of 2D/3D nano-microstructures, *iScience*, 2023, **26**, 106374.

[12] M. Marini, A. Nardini, R. Martínez Vázquez, *et al.*, Microlenses fabricated by two-photon laser polymerization for cell imaging with non-linear excitation microscopy, *Advanced Functional Materials*, 2023, **33**, 2213926.

[13] J. S. O'Neill, P. S. Salter, Z. Zhao, *et al.*, 3D switchable diffractive optical elements fabricated with two-photon polymerization, *Advanced Optical Materials*, 2022, **10**, 2102446.

[14] J. Lu, X. W. Ng, D. Piston, and T. S. Tkaczyk, Fabrication of a multifaceted mapping mirror using two-photon polymerization for a snapshot image mapping spectrometer, *Applied Optics*, 2023, **62**, 5416–5426.

[15] C. Flynn, H. Cao, B. E. Applegate, and T. S. Tkaczyk, Fabrication of waveguide directional couplers using 2-photon lithography, *Optics Express*, 2023, **31**, 26323–26334.

[16] S. Yu, Q. Du, C. R. Mendonça, L. Ranno, T. Gu, and J. Hu, Two-photon lithography for integrated photonic packaging, *Light: Advanced Manufacturing*, 2023, **4**, 32.

[17] P. S. Nair, C. Pan, H. Wang, *et al.*, Fabrication of opaque and transparent 3D structures using a single material via two-photon polymerisation lithography, *Light: Advanced Manufacturing*, 2023, **4**, 25.

[18] P. Bian, Z.-Y. Hu, X.-Q. Liu, Z.-N. Tian, and Q.-D. Chen, Laser printing high-resolution inorganic 3D microstructures, *Laser & Photonics Reviews*, 2025, **19**, e202501797.

[19] J. C. Sänger, B. R. Pauw, H. Sturm, and J. Günster, First time additively manufactured advanced ceramics by using two-photon polymerization for powder processing, *Open Ceramics*, 2020, **4**, 100040.

[20] M. Dadkhah, J.-M. Tulliani, A. Saboori, and L. Iuliano, Additive manufacturing of ceramics: Advances, challenges, and outlook, *Journal of the European Ceramic Society*, 2023, **43**, 6635–6664.

[21] G. Merkininkaitė, E. Aleksandravičius, M. Malinauskas, D. Gailevičius, and S. Šakirzanovas, Laser additive manufacturing of si/zro$_2$ tunable crystalline phase 3D nanostructures, *Opto-Electronic Advances*, 2022, **5**, 210077.

[22] D. Gailevičius, V. Padolskytė, L. Mikoliūnaitė, S. Šakirzanovas, S. Juodkazis, and M. Malinauskas, Additive-manufacturing of 3D glass-ceramics down to nanoscale resolution, *Nanoscale Horizons*, 2019, **4**, 647–651.

[23] R. Phillips, Photopolymerization, *Journal of Photochemistry*, 1984, **25**, 79–82.

[24] G. Odian, *Principles of Polymerization*. John Wiley & Sons, 4 ed., 2004.

[25] R. W. Boyd, *Nonlinear Optics*. Academic Press / Elsevier, 3rd ed., 2008.

[26] E. Skliutas, M. Lebedevaite, E. Kabouraki, *et al.*, Polymerization mechanisms initiated by spatio-temporally confined light, *Nanophotonics*, 2021, **10**, 1211–1242.

[27] M.Malinauskas, "Lecture notes on photopolymerization." Micro and Nano Fabrication Technologies.

[28] S. Zakeri, M. Vippola, and E. Levänen, A comprehensive review of the photopolymerization of ceramic resins used in stereolithography, *Additive Manufacturing*, 2020, **35**, 101177.

[29] A. Bove, F. Calignano, M. Galati, and L. Iuliano, Photopolymerization of ceramic resins by stereolithography process: A review, *Applied Sciences*, 2022, **12**, 3591.

[30] E. F. Cárdenas Correa, E. A. Torres Barahona, and J. B. Carda Castelló, Additive manufacturing of ceramic materials via direct ink writing (diw): A review, *Ceramics*, 2026, **9**.

[31] C. DOSSOU-YOVO, M. MOUGENOT, E. BEAUDROUET, *et al.*, Inkjet printing technology: A novel bottom-up approach for multilayer ceramic components and high definition printed electronic devices, *Additional Conferences (Device Packaging, HiTEC, HiTEN, CICMT)*, 2012, **2012**, 000055–000066.

[32] B. Coppola, J. Schmitt, T. Lacondemine, C. Tardivat, L. Montanaro, and P. Palmero, Digital light processing stereolithography of zirconia ceramics: Slurry elaboration and orientation-reliant mechanical properties, *Journal of the European Ceramic Society*, 2022, **42**, 2974–2982.

[33] K. G. Webber, O. Clemens, V. Buscaglia, B. Malič, R. K. Bordia, T. Fey, and U. Eckstein, Review of the opportunities and limitations for powder-based high-throughput solid-state processing of advanced functional ceramics, *Journal of the European Ceramic Society*, 2024, **44**, 116780.

[34] H. Bikas, P. Stavropoulos, and G. Chryssolouris, Additive manufacturing methods and modelling approaches: a critical review, *The International Journal of Advanced Manufacturing Technology*, 2016, **83**, 389–405.

[35] G. Merkininkaitė, E. Aleksandravičius, M. Malinauskas, D. Gailevičius, and S. Šakirzanovas, Laser additive manufacturing of si/zro₂ tunable crystalline phase 3D nanostructures, *Opto-Electronic Advances*, 2022, **5**, 210077–1–210077–11.

[36] S. O'Halloran, A. Pandit, A. Heise, and A. Kellett, Two-photon polymerization: Fundamentals, materials, and chemical modification strategies, *Advanced Science*, 2023, **10**, 2204072.

[37] G. Merkininkaite, D. Gailevicius, L. Staisiunas, E. Ezerskyte, R. Vargalis, M. Malinauskas, and S. Sakirzanovas, Additive manufacturing of sioc, sic, and si3n4 ceramic 3D microstructures, *Advanced Engineering Materials*, 2023, **25**, 2300639.

[38] J. Zha and H. Roggendorf, Sol–gel science, the physics and chemistry of sol–gel processing, ed. by c. j. brinker and g. w. scherer, academic press, boston 1990, xiv, 908 pp., bound—isbn 0-12-134970-5, *Advanced Materials*, 1991, **3**, 522–522.

[39] M. Devi, S. Rawat, and S. Sharma, A comprehensive review of the pyrolysis process: from carbon nanomaterial synthesis to waste treatment, *Oxford Open Materials Science*, 2021, **1**, itab014.

[40] R. P. Chaudhary, C. Parameswaran, M. Idrees, A. S. Rasaki, C. Liu, Z. Chen, and P. Colombo, Additive manufacturing of polymer-derived ceramics: Materials, technologies, properties and potential applications, *Progress in Materials Science*, 2022, **128**, 100969.

[41] S. Dengler and B. Eberle, Investigations on the nonlinear optical properties of 0d, 1d, and 2D boron nitride nanomaterials in the visible spectral region, *Nanomaterials*, 2023, **13**, 1849.

[42] E. Skliutas, G. Merkininkaitė, S. Maruo, *et al.*, Multiphoton 3D lithography, *Nature Reviews Methods Primers*, 2025, **5**, 15.

[43] G. Zyla and M. Farsari, Frontiers of laser-based 3D printing: A perspective on multiphoton lithography, *Laser & Photonics Reviews*, 2024, **18**, 2301312.

[44] H. Zappe, *Fundamentals of Micro-Optics*. Cambridge University Press, 2010.

[45] D. Gonzalez-Hernandez, S. Varapnickas, G. Merkininkaitė, A. Čiburys, D. Gailevicius, S. Sakirzanovas, and S. Juodkazis, Laser 3D printing of inorganic free-form micro-optics, *Photonics*, 2021, **8**, 577.

[46] S. N. Khonina, N. L. Kazanskiy, R. V. Skidanov, and M. A. Butt, Advancements and applications of diffractive optical elements in contemporary optics: A comprehensive overview, *Advanced Materials Technologies*, 2025, **10**, 2401028.

[47] D. Chekkaramkodi, L. Jacob, M. S. C, R. Umer, and H. Butt, Review of vat photopolymerization 3D printing of photonic devices, *Additive Manufacturing*, 2024, **86**, 104189.

[48] M. D. Schmid, A. Toulouse, S. Thiele, S. Mangold, A. M. Herkommer, and H. Giessen, 3D direct laser writing of highly absorptive photoresist for miniature optical apertures, *Advanced Functional Materials*, 2023, **33**, 2211159.

[49] Edvinas, "Fabrication of 3D polymeric microstructres using pulsed 3D direct laser lithography." Laboratory coursework manual.

[50] L. Jonušauskas, S. Juodkazis, and M. Malinauskas, Optical 3D printing: bridging the gaps in the mesoscale, *Journal of Optics*, 2018, **20**, 053001.

[51] Evident Corporation, *LEXT OLS5100 3D Measuring Laser Microscope: Smart Workflow, Faster Experiments*. Evident Corporation, Tokyo, Japan, 2023. Industrial brochure/manual.

[52] Olympus Corporation, *BX51 System Microscope Instruction Manual*. Olympus Corporation. Instruction manual.

[53] Thermo Fisher Scientific, *Prisma E SEM:*. SEM brochure/manual.

[54] M. Lima, R. Monteiro, M. Graça, and M. Ferreira da Silva, Structural, electrical and thermal properties of borosilicate glass–alumina composites, *Journal of Alloys and Compounds*, 2012, **538**, 66–72.

[55] I. H. Malitson, Interspecimen comparison of the refractive index of fused silica∗,†, *J. Opt. Soc. Am.*, Oct 1965, **55**, 1205–1209.

[56] D. Gailevicius, R. Zvirblis, K. Galvanauskas, G. Bataviciute, and M. Malinauskas, Calcination-enhanced laser-induced damage threshold of 3D micro-optics made with laser multi-photon lithography, *Photonics*, 2023, **10**, 597.

Acknowledgements

Firstly, I would like to thank my supervisor, Prof. Mangirdas Malinauskas, for giving me the opportunity to work on this project. The work was challenging and involved a steep learning curve for someone like me, who had no prior experience in this particular field of photonics. I am sincerely grateful for all the guidance, support, and encouragement provided throughout the year.

I would also like to thank my advisor, Dr. Greta Merkininkaitė, for always being helpful whenever assistance was needed regarding the use of the hybrid resin and the entire pyrolysis process. I am grateful for all the opportunities I received to learn not only about laser physics, but also about material science and chemistry.

Special thanks to everyone at the Laser Nanophotonics Group and the researchers at the Laser Research Center for being extremely supportive and helpful throughout the year. In particular, I would like to thank Dr. Gordon Zyla and Prof. Mikas Vengris for their patience and for helping me with the transmission measurements. I would also like to thank Artur Harnik for all the help with the SEM imaging, transmission measurements, and for helping out with my queries with chemistry. My sincere thanks also go to Dr. Mantas Gaidys, for always being available to help with the laser setup and the fabrication process. Huge thanks to Robertas Virketis from the Faculty of Chemistry as well for helping with all the pyrolysis experiments. Finally, I would like to thank my fellow students, Ioanna Angeliki Petsi, Austeja Kvedarite, and Tadas Latyvs, for their great company, support and willingness to help and guide me whenever a senior researcher was unavailable.

Last but not the least, I would like to thank my parents and my brother for their endless support throughout the course of this project, regardless of the distance. Thank you for all the encouragement and belief in me.

Fabrication Of Opaque Micrsotructures Using Multiphoton Lithography And Their Characterization

Abhinay Vats Mohan

3D laser direct writing has been employed as a technology of rapidly increasing importance finding its applications in various fields, especially in micro-optics, with a growing demand for transparent and opaque three dimensional microstructures, where opaque microelements play essential roles, especially for stray light suppression, beam blocking and beam absorption. While Two Photon Polymerization (TPP) enables the fabrication of complex, high resolution free-form 3D structures, the construction of opaque microstructures remains challenging, due to the strong absorption of opaque photoresists in the UV to near-infrared spectral regime. Moreover, most of the previous demonstrations of opaque microstructures have been achieved using organic photoresists, which limit the mechanical and thermal performance of the fabricated components.

The aim of this work is to fabricate true 3D microstructures using a hybrid organic-inorganic resist via multiphoton lithography and to characterize their optical opacity after pyrolysis.

The introduction of the work is provided first, followed by a review of the published literature in Section 1, which explains both the physical phenomena of the fabrication process, and also provides an overview of the opaque microstructures as well. A description of the experimental methods used in the study is explained, where the general workflow followed for the fabrication and characterization of the structures is described in detail. The next section introduces the design for the actual experiments performed, where the experimental setup along with the parameters used are explained thoroughly, from the fabrication, pyrolysis, and finally characterization of the structures. In Section 4, all the results obtained are presented and discussed, following the same order as that of the previous section. It includes the optimization of the laser parameters during the fabrication process, followed by the attempts made to obtain the opaque microstructures post pyrolysis, and finally a detailed description of the opacity tests performed on the structures, characterizing them as strongly absorbent.

At last, a small comparison with literature along with scope for future works is provided in the last sections, which show sufficient voxel overlap is essential for the fabrication of solid microstructures, the surface quality of the structures can be improved post pyrolysis provided the structures undergo sufficient cross-linking, and the pyrolyzed structures obtained strongly absorb light in the visible spectrum, surpassing the previously reported values while realizing them as even shorter structures.

मल्टीफोटॉन लिथोग्राफी का उपयोग करके अपारदर्शी माइक्रोस्ट्रक्चर्स का निर्माण तथा उनका विश्लेषण

अभिनय वत्स मोहन

त्रिआयामी लेज़र डायरेक्ट राइटिंग एक तीव्र गति से विकसित होने वाली तकनीक के रूप में उभरी है, जिसका उपयोग विभिन्न क्षेत्रों में किया जा रहा है, विशेष रूप से माइक्रो-ऑप्टिक्स में। इस क्षेत्र में पारदर्शी तथा अपारदर्शी त्रि-आयामी माइक्रोस्ट्रक्चर्स की मांग लगातार बढ़ रही है, जहाँ अपारदर्शी माइक्रोएलिमेंट्स विशेष रूप से स्ट्रे लाइट दमन, बीम ब्लॉकिंग तथा बीम अवशोषण में महत्वपूर्ण भूमिका निभाते हैं। यद्यपि टू-फोटॉन पॉलिमराइज़ेशन जटिल, उच्च-रिज़ॉल्यूशन तथा फ्री-फॉर्म त्रिआयामी संरचनाओं के निर्माण को संभव बनाता है, फिर भी अपारदर्शी माइक्रोस्ट्रक्चर्स का निर्माण चुनौतीपूर्ण बना हुआ है, क्योंकि अपारदर्शी फोटोरेज़िस्ट पराबैंगनी से लेकर निकट-अवरक्त स्पेक्ट्रल क्षेत्र में अत्यधिक अवशोषण प्रदर्शित करते हैं। इसके अतिरिक्त, अब तक अपारदर्शी माइक्रोस्ट्रक्चर्स के अधिकांश प्रदर्शन ऑर्गेनिक फोटोरेज़िस्ट्स का उपयोग करके प्राप्त किए गए हैं, जो निर्मित घटकों के यांत्रिक तथा तापीय प्रदर्शन को सीमित करते हैं।

इस कार्य का उद्देश्य मल्टीफोटॉन लिथोग्राफी का उपयोग करके एक हाइब्रिड ऑर्गेनिक-इनऑर्गेनिक रेज़िस्ट से वास्तविक त्रिआयामी माइक्रोस्ट्रक्चर्स का निर्माण करना तथा पाइरोलिसिस के बाद उनकी ऑप्टिकल अपारदर्शिता का विश्लेषण करना है।

कार्य की शुरुआत परिचय से की गई है, जिसके बाद अनुभाग एक में प्रकाशित साहित्य की समीक्षा प्रस्तुत की गई है। इसमें निर्माण प्रक्रिया से संबंधित भौतिक घटनाओं की व्याख्या के साथ-साथ अपारदर्शी माइक्रोस्ट्रक्चर्स का अवलोकन भी प्रदान किया गया है। इसके पश्चात अध्ययन में उपयोग की गई प्रायोगिक विधियों का वर्णन किया गया है, जहाँ संरचनाओं के निर्माण तथा उनके विश्लेषण के लिए अपनाई गई सामान्य कार्यप्रणाली को विस्तारपूर्वक समझाया गया है।

अगला अनुभाग वास्तविक प्रयोगों की रूपरेखा प्रस्तुत करता है, जिसमें प्रयोगात्मक सेटअप तथा उपयोग किए गए सभी पैरामीटर्स का विस्तृत वर्णन किया गया है, जिसमें संरचनाओं के निर्माण, पाइरोलिसिस तथा अंततः उनके विश्लेषण तक की पूरी प्रक्रिया शामिल है। अनुभाग चार में प्राप्त सभी परिणामों को प्रस्तुत और चर्चा की गई है, उसी क्रम का पालन करते हुए जैसा पिछले अनुभाग में दिया गया था। इसमें निर्माण प्रक्रिया के दौरान लेज़र पैरामीटर्स का अनुकूलन, पाइरोलिसिस के बाद अपारदर्शी माइक्रोस्ट्रक्चर्स प्राप्त करने के प्रयास, तथा अंततः संरचनाओं पर किए गए अपारदर्शिता परीक्षणों का विस्तृत विवरण शामिल है, जिन्होंने इन संरचनाओं को अत्यधिक प्रकाश-अवशोषक सिद्ध किया।

अंत में, साहित्य के साथ एक संक्षिप्त तुलना तथा भविष्य के कार्यों की संभावनाओं पर चर्चा प्रस्तुत की गई है। परिणाम दर्शाते हैं कि ठोस माइक्रोस्ट्रक्चर्स के निर्माण के लिए पर्याप्त वॉक्सेल ओवरलैप अत्यंत आवश्यक है, पाइरोलिसिस के बाद संरचनाओं की सतही गुणवत्ता में सुधार किया जा सकता है यदि संरचनाएँ पर्याप्त क्रॉस-लिंकिंग से गुजरें, तथा प्राप्त पाइरोलाइज़्ड संरचनाएँ दृश्य स्पेक्ट्रम में प्रकाश का अत्यधिक अवशोषण प्रदर्शित करती हैं, जो पूर्व प्रकाशित परिणामों की तुलना में बेहतर है, जबकि यह व्यवहार अपेक्षाकृत कम संरचनात्मक मोटाई पर प्राप्त किया गया।